JGR Solid Earth

RESEARCH ARTICLE
10.1029/2021JB023027

Magnetic Domain State and Anisotropy in Hematite (α-Fe_2O_3) From First-Order Reversal Curve Diagrams

Andrew P. Roberts[1,2], Xiang Zhao[1,2], Pengxiang Hu[1,2], Alexandra Abrajevitch[3], Yen-Hua Chen[4], Richard J. Harrison[5], David Heslop[1,2], Zhaoxia Jiang[6], Jinhua Li[7], Qingsong Liu[8], Adrian R. Muxworthy[9], Hirokuni Oda[2], Hugh St. C. O'Neill[10], Brad J. Pillans[1], and Tetsuro Sato[2,11]

[1]Research School of Earth Sciences, Australian National University, Canberra, ACT, Australia, [2]Research Institute of Geology and Geoinformation, Geological Survey of Japan, National Institute of Advanced Industrial Science and Technology, Tsukuba, Japan, [3]Institute of Tectonics and Geophysics, Russian Academy of Sciences, Khabarovsk, Russia, [4]Department of Earth Sciences, National Cheng Kung University, Tainan, Taiwan, [5]Department of Earth Sciences, University of Cambridge, Cambridge, UK, [6]Key Laboratory of Submarine Geosciences and Prospecting Techniques, Ministry of Education, and College of Marine Geosciences, Ocean University of China, Qingdao, China, [7]Key Laboratory of Earth and Planetary Physics, Institute of Geology and Geophysics, Chinese Academy of Sciences, Beijing, China, [8]Centre for Marine Magnetism, Department of Ocean Science and Engineering, Southern University of Science and Technology, Shenzhen, China, [9]Department of Earth Science and Engineering, Imperial College London, London, UK, [10]School of Earth, Atmosphere and Environment, Monash University, Clayton, VIC, Australia, [11]Earthquake Research Institute, University of Tokyo, Tokyo, Japan

Key Points:

- FORC diagrams are presented for diverse natural and synthetic hematite samples to demonstrate domain state and anisotropy signatures
- Kidney-shaped FORC distributions are indicative of multiaxial anisotropy and central ridge-type distributions reflect uniaxial anisotropy
- The dominant FORC distribution type depends on the balance between uniaxial and triaxial switching mechanisms

Correspondence to:
A. P. Roberts,
andrew.roberts@anu.edu.au

Citation:
Roberts, A. P., Zhao, X., Hu, P., Abrajevitch, A., Chen, Y.-H., Harrison, R. J., et al. (2021). Magnetic domain state and anisotropy in hematite (α-Fe_2O_3) from first-order reversal curve diagrams. *Journal of Geophysical Research: Solid Earth*, *126*, e2021JB023027. https://doi.org/10.1029/2021JB023027

Received 12 AUG 2021
Accepted 20 NOV 2021

Abstract Hematite carries magnetic signals of interest in tectonic, paleoclimatic, paleomagnetic, and planetary studies. First-order reversal curve (FORC) diagrams have become an important tool for assessing the domain state of, and magnetostatic interactions among, magnetic particles in such studies. We present here FORC diagrams for diverse hematite samples, which provide a catalog for comparison with other studies and explain key features observed for hematite. Ridge-type signatures typical of uniaxial single-domain particle assemblages and "kidney-shaped" FORC signatures, and combinations of these responses, occur commonly in natural and synthetic hematite. Asymmetric features that arise from the triaxial basal plane anisotropy of hematite contribute to vertical spreading in kidney-shaped FORC distributions and are intrinsic responses even for magnetostatically noninteracting particles. The dominant FORC distribution type in a sample (ridge, kidney-shaped, or mixture) depends on the balance between uniaxial/triaxial switching. The identified signals explain magnetization switching and anisotropy features that are intrinsic to the magnetic properties of hematite and other materials with multiaxial magnetic anisotropy.

Plain Language Summary First-order reversal curve (FORC) diagrams have become a standard method for identifying the domain state of magnetic materials. It has recently been demonstrated that the magnetic anisotropy type can also be identified using FORC diagrams. The magnetic domain state and anisotropy type of a magnetic mineral control the fidelity of recording of magnetic information, so identifying these features is fundamental to paleomagnetic, rock magnetic, and environmental magnetic studies. Hematite is a naturally abundant magnetic mineral that is encountered commonly in such studies, so it is important to have extensive FORC reference data for this mineral. We present the most comprehensive available FORC study of diverse natural and synthetic hematite samples, including numerical simulation results, to seek to explain key domain state and anisotropy signals for hematite.

1. Introduction

Hematite (α-Fe_2O_3) is a naturally abundant and important magnetic mineral in paleomagnetism, rock magnetism, and environmental magnetism. Although its magnetic properties have been investigated extensively, first-order reversal curve (FORC) diagrams (Pike et al., 1999; Roberts et al., 2000) have yet to be studied in detail for hematite even though FORC diagrams are now a standard tool for characterizing magnetic domain states and magnetostatic interactions. FORC diagrams for hematite have been reported widely (Abrajevitch et al., 2014; Brownlee et al., 2011; Carvallo et al., 2006; Carvallo & Muxworthy, 2006; Church et al., 2016; Hu et al., 2021; Jiang et al., 2016; Jovane et al., 2011; Liu et al., 2010; Martín-Hernández & Guerrero-Suárez, 2012; Muxworthy et al., 2005; Pariona et al., 2016; Pike et al., 2001; Roberts et al., 2006; Zhao et al., 2017), although individual

studies have mainly not documented diverse FORC behavior in hematite. Contrasting FORC distributions have been reported for different natural and synthetic samples, the origins of which remain largely unexplained. Additionally, detailed results for the more extensive FORC-type measurements of Zhao et al. (2017) have yet to be reported for hematite.

We present results here for conventional and extended FORC measurements of Zhao et al. (2017) for diverse natural and synthetic hematite samples. In addition to enabling magnetostatic interaction and domain state identification (Roberts et al., 2014), FORC diagrams contain valuable information about the controlling magnetic anisotropy in magnetic materials (Egli, 2021; Harrison et al., 2019; Harrison & Lascu, 2014; Valdez-Grijalva et al., 2018; Valdez-Grijalva & Muxworthy, 2019). We discuss these information types here and seek to explain diverse FORC signals for hematite using the numerical simulations of Harrison et al. (2019). Our extensive FORC data for hematite will be valuable for comparing with other studies and provide a data library for diverse samples that can help to train FORC unmixing algorithms via machine learning.

Ensuring that samples contain only a single magnetic phase is especially important for illustrating the FORC properties of hematite because the saturation magnetization (M_s) of hematite is ~1/200th that of magnetite (~0.4 $Am^2\ kg^{-1}$ (de Boer et al., 2001) compared to ~92 $Am^2\ kg^{-1}$). Even minor magnetite and/or maghemite impurities can dominate measured magnetic properties (e.g., Dekkers, 1990; Frank & Nowaczyk, 2008; Roberts et al., 2020). We present additional information as relevant to demonstrate that hematite is the only magnetic phase present in the studied samples.

2. Crystal Structure and Magnetism in Hematite

Various crystallographic and magnetic factors are important when considering the magnetic properties of hematite. These factors are outlined here and are discussed further below where relevant to our experimental results.

2.1. Crystal Structure

Hematite has a corundum (Al_2O_3) structure (space group $R\bar{3}c$, $Z = 6$) and can be indexed with rhombohedral or hexagonal (Figure 1) unit cells. Here we refer all directions and planes to the hexagonal cell. Hematite consists of hexagonally close packed O^{2-} arrays stacked along the [001] direction. Fe^{3+} ions occupy two-thirds of octahedral sites to form symmetrically equivalent layers parallel to the (001) plane (Figure 1a). O^{2-} ions are packed with slight distortion. The cation arrangement produces pairs of $Fe(O)_6$ octahedra, with each octahedron sharing edges with three neighboring octahedra in the same plane. One face is shared with an octahedron in the adjacent plane along the c-axis (Figure 1b), which causes a distortion from ideal cation packing (Cornell & Schwertmann, 2003). The Fe-O_3-Fe triplet structure (Figure 1a) is responsible for the superexchange that produces the magnetism of hematite (Robinson et al., 2004; Samuelson & Shirane, 1970).

2.2. Magnetic Structure

Hematite has an antiferromagnetic structure at room temperature with moments in the (001) plane (Shull et al., 1951). Magnetic moments of Fe^{3+} ions have the same orientation within a single basal plane (i.e., with ferromagnetic coupling); alternating antiparallel alignment of moments in pairs of planes gives rise to antiferromagnetic coupling. Dzyaloshinsky (1958) demonstrated that hematite occurs in two antiferromagnetic states at different temperatures. Below the Morin (1950) transition temperature, T_M (~260 K), spins lie nearly parallel to the crystallographic c axis (i.e., perpendicular to the basal plane) and hematite is antiferromagnetic with fully compensated sublattice moments so that the spontaneous magnetization disappears. Between T_M and the Néel temperature, T_N, spins lie close to the basal plane nearly perpendicular to one of the three <100> crystallographic axes of the hexagonal unit cell and nearly parallel to a $\{11\bar{2}0\}$ mirror plane (normal to the corresponding <100> direction). The antiferromagnetic alignment axis can rotate by up to 20° out of the basal plane about the <100> axis (Brok et al., 2017). Independently, slight spin canting away from the $\{11\bar{2}0\}$ mirror plane produces a weak canted antiferromagnetism with a net moment strictly parallel to the corresponding <100> axis, that is, exactly within the basal plane (Dzyaloshinsky, 1958). Moriya (1960) analyzed this spin canting in terms of anisotropic superexchange coupling in hematite and concluded that spin-orbit coupling is responsible for the slight spin

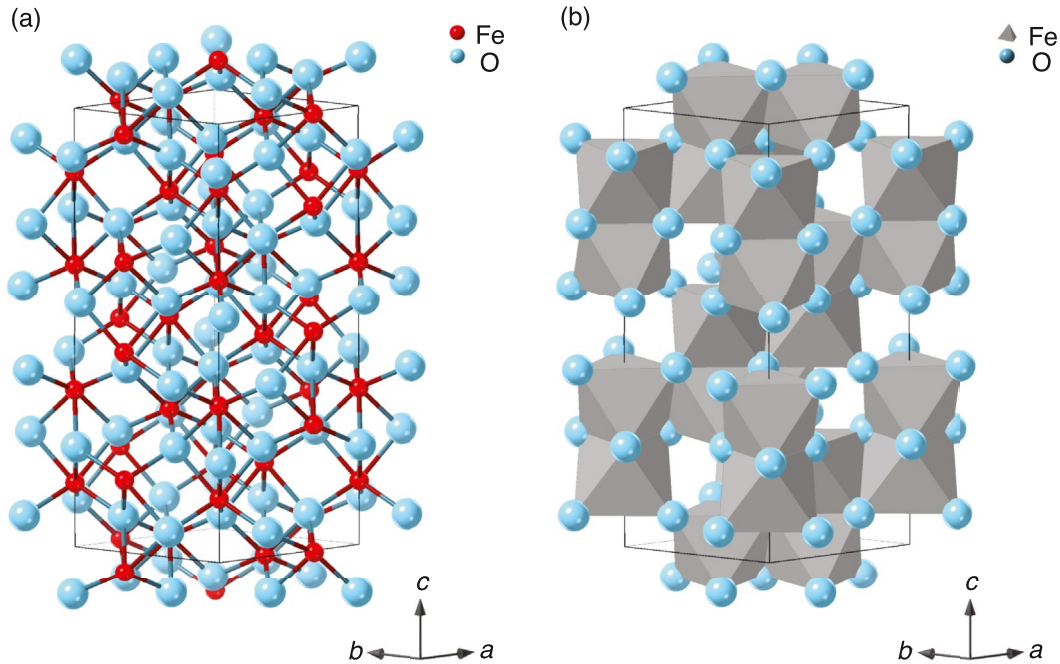

Figure 1. Crystal structure of hematite. (a) Ball and stick and (b) coordination polyhedral representations of the atomic arrangement within a hexagonal unit cell (thin black line), with $a = 5.0380$ Å and $c = 13.7720$ Å. Images were made with the CrystalMaker software.

canting of 10^{-3} radians (0.057°). The tiny canting angle explains why hematite has a weak spontaneous moment of only a few percent of the moment of a Fe^{3+} atom and ~0.5% of the value of magnetite.

In addition to a net magnetization due to canted antiferromagnetism, a defect moment, which arises from disruptions of the canted antiferromagnetic structure, is generally present in hematite. Defect moments result from stacking faults within the crystal lattice (Néel, 1953), vacancies due to missing cations, or substitution of other cations with no net moment or with a different moment to a Fe^{3+} cation. A third magnetization source due to disordered surface spins (e.g., Bødker et al., 2000) can be important in <30 nm particles, where the volumetric contribution of surface moments is more significant in nanoparticles than in larger particles (Dormann et al., 1997; Kodama, 1999).

2.3. Anisotropy

The weak M_s of hematite means that shape anisotropy cannot explain its large coercivity even for highly acicular particles (Stacey & Banerjee, 1974). Tasaki and Iida (1963) demonstrated that hematite has triaxial basal plane anisotropy, with sixfold symmetry, which is consistent with its crystal symmetry (see Fabian et al. (2011) and Figures 2a–2c), but the amplitude of their measured ferromagnetic resonance fields was too small for triaxial basal plane anisotropy to control the coercivity of SD hematite (Banerjee, 1963). Experiments with stressed individual hematite crystals indicate that their coercivity is instead controlled by internal stresses (Mizushima & Iida, 1966; Porath, 1968; Porath & Raleigh, 1967; Stacey & Banerjee, 1974; Sunagawa & Flanders, 1965). The main coercivity source in hematite is, thus, magnetoelastic anisotropy associated with dislocations, defects, or internal strains in nanoparticles because neither magnetocrystalline nor shape anisotropy can explain observed coercivities (Özdemir & Dunlop, 2014). Correlation of the coercive force (B_c) with the defect moment in synthetic and natural particles is consistent with internal strain explaining the coercivity of hematite (Özdemir & Dunlop, 2014). The high magnetostriction of hematite (Urquhart & Goldman, 1956) and weak M_s suggests a high sensitivity to magnetostrictive strain in hematite (Banerjee, 1963). Strain-related anisotropy in hematite is taken to be uniaxial.

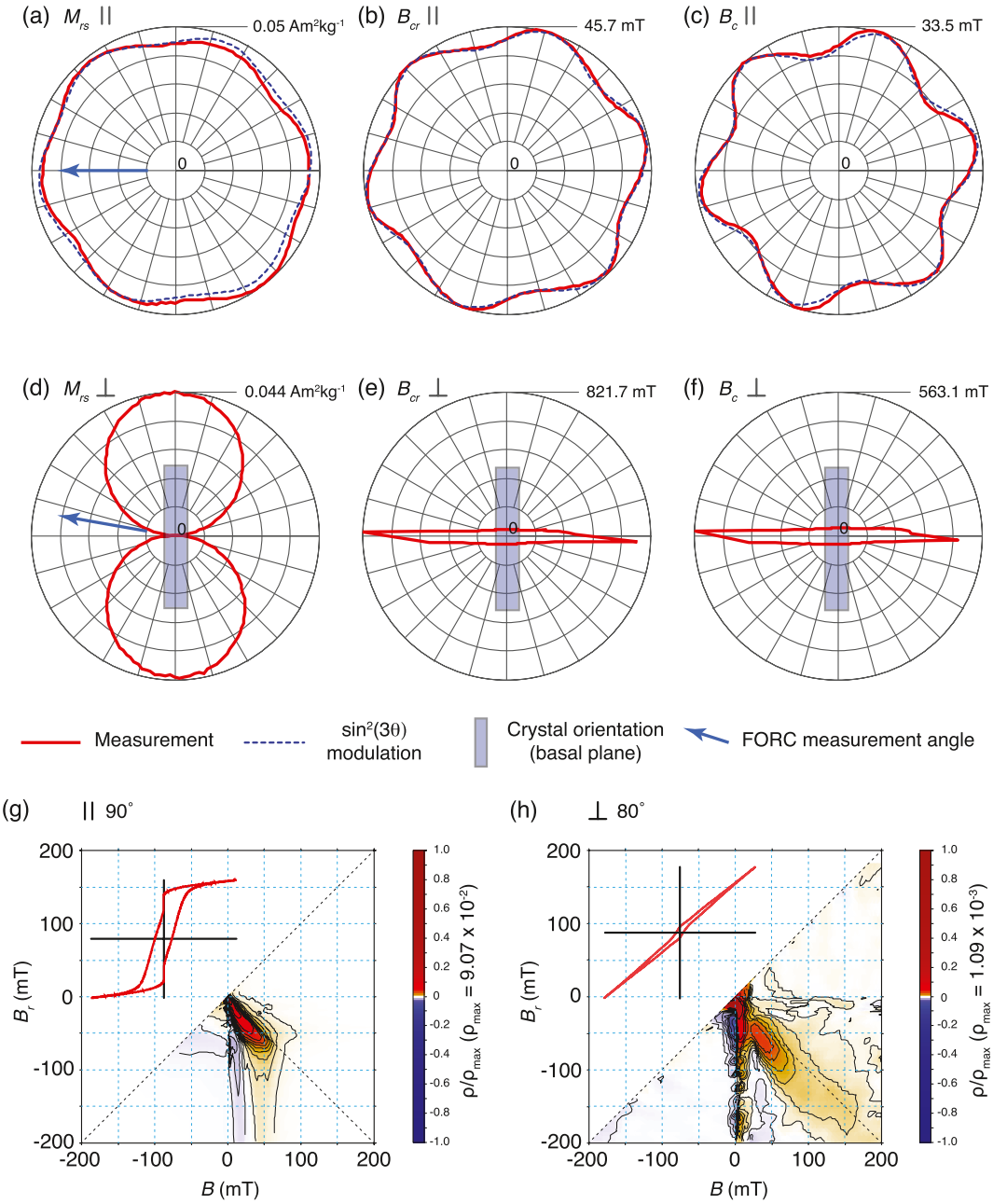

Figure 2. M_{rs}, B_{cr}, and B_c variations in a 5-mm single hematite crystal fragment (a–c) parallel and (d–f) perpendicular to the basal plane of the crystal. FORC diagrams are shown (g) parallel and (h) nearly perpendicular (at ~80°) to the basal plane of the crystal (orientations of FORC measurements with respect to the crystal are indicated by arrows in [a] and [d]). In-plane results in (a–c) have a periodicity ($\sin^2(3\theta)$) that reflects triaxial basal plane anisotropy, while results perpendicular to the basal plane (d–f) reflect uniaxial anisotropy ($\sin^2\theta$). The measured crystal fragment did not have hexagonal boundaries to enable orientation of measurements along crystallographic axes, so the measurement orientations are arbitrary. Easy magnetization axes align with the three crystallographic *a*-axes (Wohlfarth, 1955); maximum M_{rs}, B_{cr}, and B_c values are indicated and occur when *a*-axes are parallel to the applied field (Fabian et al., 2011).

Triaxial and uniaxial anisotropy are important for interpreting FORC diagrams for hematite. Internal stresses and/or defects produce an induced uniaxial anisotropy (K_u). The out-of-plane component of intrinsic magnetocrystalline anisotropy (K_1) is also uniaxial (e.g., Figures 2d–2f), and the in-plane component (K_3) has triaxial magnetocrystalline anisotropy (e.g., Figures 2a–2c). The anisotropy energy (E_{an}) for hematite can be approximated

by combining these sources, with uniaxial and triaxial terms given, respectively, by $K\sin^2\theta$ (Cullity, 1972) and $K\sin^2(3\theta)$ (Dunlop, 1971):

$$E_{an} = K_u \sin^2\theta + K_1 \sin^2\phi + K_3 \sin^2(3\theta), \quad (1)$$

where θ is the angle of the magnetization with respect to the basal plane easy axis and ϕ is its out-of-plane angle with respect to the basal plane. The balance between K_u, K_1, and K_3 determines the nature of FORC diagrams for hematite, as discussed below.

2.4. Domain State Threshold Sizes

The particle sizes of transitions between magnetic domain states are critically important for understanding magnetic recording and for interpreting FORC diagrams. The superparamagnetic (SP) to stable single domain (SD) threshold size for hematite is estimated at 25–30 nm (Banerjee, 1971; Özdemir & Dunlop, 2014). This threshold size occurs at 17 nm for Al-hematite (Jiang et al., 2014), with enhanced magnetic stability of Al-hematite compared to stoichiometric hematite attributed to greater lattice distortion when Al^{3+} substitutes into the crystal lattice for Fe^{3+} (Jiang et al., 2014). Banerjee (1971) proposed that the SD to multidomain (MD) threshold (i.e., the upper size limit for magnetization reversal via coherent rotation) for hematite occurs at ~15 μm, while Kletetschka and Wasilewski (2002) suggested a transition from quasi-stable SD to true MD behavior at 100 μm. Özdemir and Dunlop (2014) suggested from a compilation of B_c values that the proposed thresholds of 15 and 100 μm are both questionable and that the SD to MD threshold likely exceeds 15 μm, with no strong evidence for such a threshold at ~100 μm. The size at which this threshold occurs remains an open question (Özdemir & Dunlop, 2014). The large size range for stable SD behavior in hematite (~28 nm to tens of microns) means that most hematite encountered in paleomagnetic and environmental magnetic studies is likely to be in the SP to SD size range.

2.5. Magnetic Hysteresis

Stoner and Wohlfarth (1948) theory is used widely to understand the hysteresis behavior of randomly oriented uniaxial SD particle assemblages. Dunlop (1971) extended this theory for randomly oriented SD hematite particles by assuming that magnetization reversal occurs by coherent rotation and that the magnetization is confined to the basal plane (except near saturation). Dunlop (1971) considered two extreme cases: (a) the applied field is large enough to overcome all energy barriers in the basal plane but is incapable of pulling the magnetic moment significantly out of the basal plane, and (b) the magnetic moment is pulled out of the basal plane into alignment with the field. The basal plane magnetocrystalline anisotropy of hematite is triaxial with two potential orientations for each easy axis so that it has sixfold symmetry (Figures 2a–2c). Dunlop (1971) calculated that $M_{rs}/M_s = 0.75$ for case (a) and $M_{rs}/M_s = 0.955$ for case (b). M_{rs}/M_s values, therefore, provide an important indicator of multi-axial anisotropies; for uniaxial anisotropy, M_{rs}/M_s is almost always less than the theoretical Stoner and Wohlfarth (1948) value of 0.5 for natural samples (e.g., Roberts et al., 2012). Anderson et al. (1954) argued that a 3 T field is required to pull the magnetization of hematite out of the basal plane and into the *c*-axis, so Dunlop (1971) suggested that $M_{rs}/M_s = 0.75$ is more likely for randomly oriented hematite particles. Thermal activation lowers M_{rs}/M_s in natural hematite assemblages, which generally varies between 0.5 and 0.75 (Özdemir & Dunlop, 2014). MD hematite often has higher M_{rs}/M_s values (0.5–0.9) than SD hematite (Özdemir & Dunlop, 2014). These considerations are important for understanding hysteresis and FORC results for hematite.

3. Samples

Results are presented here for diverse natural and synthetic hematite nanoparticle samples. Synthetic samples are described first, along with available mineralogical and particle size characterizations, followed by the natural samples, with relevant properties summarized in Table 1.

3.1. Synthetic Samples

Pure synthetic hematite nanoparticles were produced with a range of methods. Sample HFh0 was produced by transforming an initial ferrihydrite to hematite, where H indicates hematite, Fh indicates ferrihydrite, and 0

Table 1
Summary of Sample Characteristics, Including Dominant FORC Anisotropy Type

Sample	Sample type	Sample preparation	Grain size (nm)	Anisotropy type	Figures
LAN45	Regolith	Natural	ND	Multiaxial	5a
LAN44	Regolith	Natural	ND	Multiaxial	5b
LAN43	Regolith	Natural	ND	Multiaxial	5c
LAN1	Regolith	Natural	ND	Multiaxial	5d
LAN70	Regolith	Natural	ND	Multiaxial	5e
LAN9	Regolith	Natural	$(\sim 3–7) \times 10^3$	Multiaxial	5f, 9e
LAN5	Regolith	Natural	ND	Multiaxial	5g
LAN3	Regolith	Natural	ND	Multiaxial	5h
LAN72	Regolith	Natural	ND	Mixed	5i
LAN4	Regolith	Natural	ND	Mixed	5j
LAN8	Regolith	Natural	ND	Uniaxial	5k
STB2	Regolith	Natural	ND	Uniaxial	5l
HGL20	Synthetic	From goethite	32 ± 7	ND	6a
Particles	Synthetic	Hydrothermal	45–85	Uniaxial	6b
Rods	Synthetic	Hydrothermal	250-350 (l) 50–100 (w)	Uniaxial	6c
HFh0	Synthetic	From ferrihydrite	167 ± 50	Uniaxial	6d
HGH0	Synthetic	From goethite	229 ± 77	Multiaxial	6e
HGL0	Synthetic	From goethite	249 ± 81	Multiaxial	6f
$F_{73.2\ mT}$	Synthetic	From ferrihydrite	~260	Uniaxial	6g
$F_{101.6\ mT}$	Synthetic	From ferrihydrite	~260	Uniaxial	6h
$F_{104.4\ mT}$	Synthetic	From ferrihydrite	~260	Uniaxial	6i
HSCO1	Synthetic	High-T flux	$(\sim 10–30) \times 10^3$	Multiaxial	6j
HSCO5	Synthetic	High-T flux	$(\sim 30–150) \times 10^3$	Multiaxial	9i
HA1	Concretion	Natural	ND	Mixed	7a
HA2	Iron ore	Natural	ND	Mixed	7b
Zebra red	Hydrothermal pigment	Natural	ND	Mixed	8
A31-36426	Crystal fragment	Natural	$\sim 5 \times 10^6$	Multiaxial	2g, 2h, 9a

Note. ND, not determined; High-T, high-temperature.

indicates the initial mol% Al content. Sample HFh0 was produced by mixing 100 ml of 0.4 M $Fe(NO_3)_3$ with 1 M NaOH to a final pH of 9. To prevent goethite formation after precipitation, L-tartrate was added immediately with 8×10^{-4} M concentration and the ferrihydrite suspension was aged in an oven at 95°C (Jiang et al., 2012). Samples HGH0 and HGL0 were produced by thermal dehydration of an initial goethite to hematite, where the first H indicates hematite, 0 indicates the initial mol% Al content, G indicates the goethite precursor, and the second H or L indicate high or low crystallinity, respectively. Hematite was synthesized from the initial goethite either by aging a Fe^{3+} salt in 5 M NaOH at 60°C (HGH* series) or by precipitating and oxidizing a Fe^{2+} salt at room temperature (HGL* series) (Jiang et al., 2012). The hematite end-member samples (0 mol. % Al) are discussed here and have lattice parameters and particle sizes as follows (Jiang et al., 2012): HFh0 ($a = 0.5037$ nm, $c = 1.3788$ nm; 167 ± 50 nm (1σ); Figure 3a), HGH0 ($a = 0.5020$ nm, $c = 1.3701$ nm; 229 ± 77 nm; Figure 3b), and HGL0 ($a = 0.5014$ nm, $c = 1.3690$ nm; 249 ± 81 nm; Figure 3c). In addition to pure end member hematite, we discuss results for the finer-grained sample HGL20, which was prepared by dehydrating goethite at 800°C for 4 hr; the initial goethite was produced in 1 liter of 0.04 M $FeSO_4$, 0.01 M $Al(NO_3)_3$, and 110 ml of 1 M $NaHCO_3$ at 800°C for 4 hr (Jiang et al., 2012). Sample HGL20 has 15.8 mol% Al, $a = 0.4976$ nm, $c = 1.3696$ nm, and 32 ± 7 nm particle size (Jiang et al., 2012).

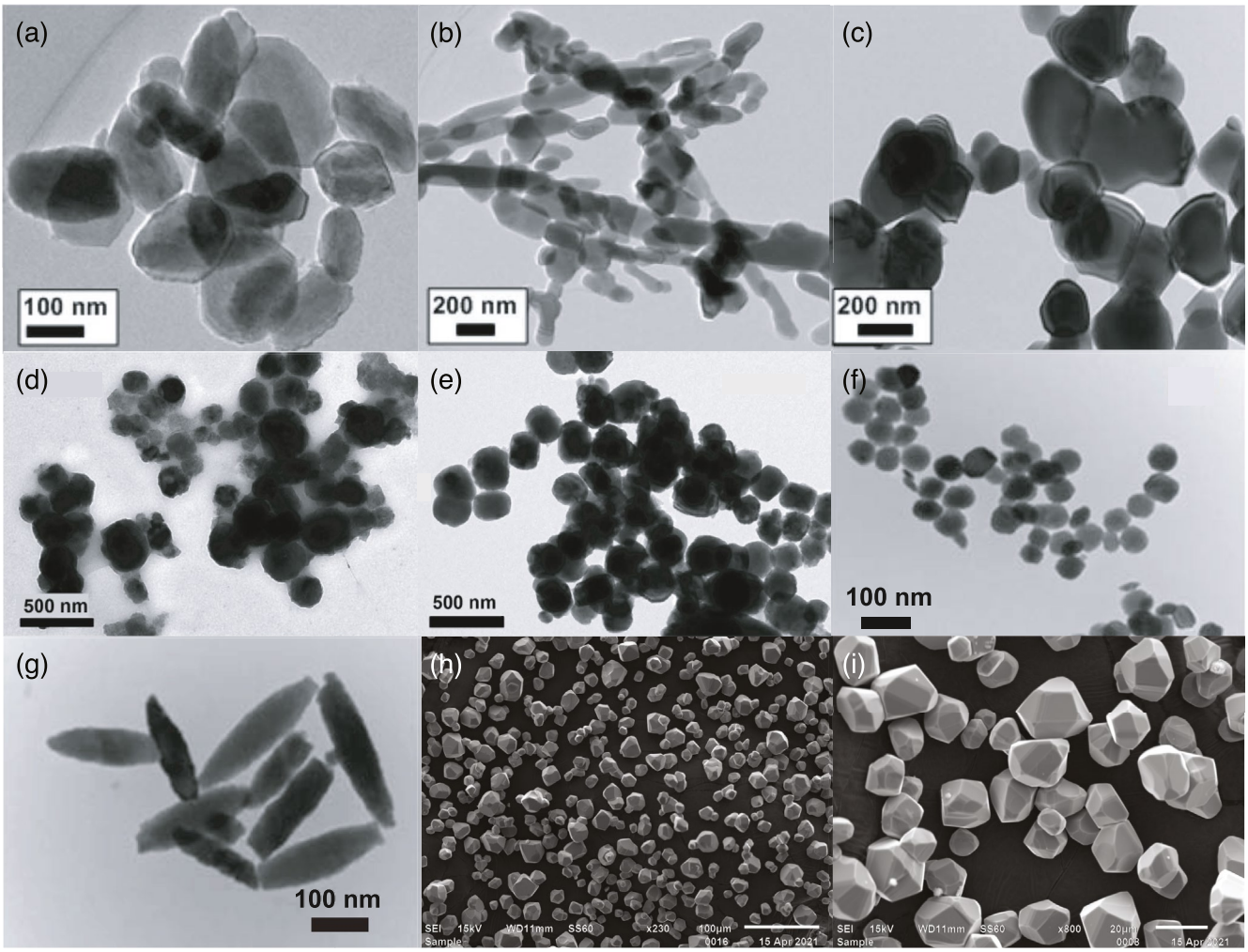

Figure 3. Transmission electron microscope (TEM) and scanning electron microscope (SEM) images of the synthetic hematite samples. TEM images are for samples: (a) HFh0, (b) HGH0, and (c) HGL0 from Jiang et al. (2012), (d) $F_{73.2\,\mu T}$ and (e) $F_{104.4\,\mu T}$ from Jiang et al. (2016), and (f) nanoparticle and (g) nanorod samples from Chen and Lin (2014). (h, i) SEM images for sample HSCO1 (this study; 100 and 20 μm scale bars, respectively).

Another synthetic hematite sample series was produced by transforming initial ferrihydrite in different magnetic fields (Jiang et al., 2016). Ferrihydrite was synthesized by mixing 100 ml of 0.5 M $Fe(NO_3)_3$ and 100 ml of 2 M NaOH at room temperature; 50 ml of 1 M $NaHCO_3$ was then added to bring the pH to ~7 at room temperature. Deionized water was used and was heated to 95°C before use to inhibit goethite formation. Resulting suspensions were heated at 95°C with variable magnetic fields produced in a set of 1 × 1 × 1 m Helmholtz coils aligned along the ambient laboratory field declination. The hematite samples discussed here were produced in applied fields of 73.2 μT, 101.6 μT, and 104.4 μT, and are labeled as samples $F_{73.2\,\mu T}$ (Figure 3d), $F_{101.6\,\mu T}$ (Figure 3e), and $F_{104.4\,\mu T}$, respectively, with consistent particle sizes of 260 nm (Jiang et al., 2016).

Further equidimensional hematite nanoparticles were synthesized hydrothermally by mixing a 0.046 M $Fe(NO_3)_3{\cdot}9H_2O$ solution and a 0.002 M $NaH_2PO_4{\cdot}2H_2O$ solution and stirring for 15 min (Islam et al., 2012). The solution was then placed in an autoclave, heated at 220°C for 48 hr, and cooled to room temperature (RT). The precipitates were separated magnetically from the mother liquor, washed with deionized water, dried at 60°C for 6 hr, and cooled to RT to yield hematite nanoparticles with 45–85 nm sizes (Figure 3f). Hematite nanorod samples were synthesized by mixing 0.02 M $FeCl_3$ and 7.4×10^{-4} M $NH_4H_2PO_4$ and stirring for 15 min (Islam et al., 2012). The solution was placed in an autoclave and heated at 220°C for 6 hr. Precipitates were separated from the mother liquor by centrifugation and were dried in an oven at 60°C for 6 hr to obtain hematite nanorods

with particle sizes of 250–350 nm (length) × 50–100 nm (width) (Figure 3g). Details of the hematite precipitates produced with this method are presented by Chen and Lin (2014).

Two coarse synthetic hematite samples (HSCO1, HSCO5) were produced by the flux method with different solvents. Sample HSCO1 consists of well-crystallized ~10–30 μm α-Fe_2O_3 (Figures 3h and 3i) that was prepared from a solvent consisting of 22 g Na_2WO_4 and 4 g WO_3 (O'Neill et al., 1992) that was mixed with 6 g α-Fe_2O_3 and homogenized by grinding in an agate mortar. The mixture was placed in a platinum crucible with a loose fitting Pt lid and was heated in a box furnace in air, initially over several hours in ~100°C steps to 700°C to ensure that moisture was removed before the flux melted, and then to 1,250°C. After 3 hrs at 1,250°C, the furnace was cooled to 900°C at 10°C/hr. The crucibles were then removed from the furnace and cooled to room temperature; flux was removed by dissolution in warm water in an ultrasonic bath. Water was decanted off and replaced several times, which removed any fine material. Sample HSCO5 was prepared with $Na_2B_4O_7$ flux following Chase and Morse (1973) with a molar ratio of 0.6 $Na_2B_4O_7$ to 0.4 α-Fe_2O_3 from a starting mix of $Na_2B_4O_7.10H_2O$. As above, the mixture was heated in a Pt crucible in air to 1,260°C to remove H_2O below the solidus, and was then cooled at 2°C/hr to 1,040°C, removed from the furnace, and the flux dissolved in warm nitric acid to produce ~30–150 μm crystals.

3.2. Natural Samples

Natural hematite-bearing samples were obtained from deeply weathered regolith from Lancefield South gold mine (LAN) near Laverton, Western Australia (WA), and St Barbara gold mine (STB), Meekatharra, WA. Regolith formation in the Yilgarn Craton, WA, has caused weatherable minerals to alter to kaolinite, goethite, and hematite (Anand & Butt, 2010). As discussed below, hematite is the only magnetic mineral detected in these samples. Magnetite and maghemite are straightforward to identify in FORC diagrams; occasional maghemite occurrences were excluded from the results discussed here. Results for regolith samples are presented to illustrate FORC results for natural pigmentary hematite with variable properties. Other diverse natural hematite-bearing samples were also analyzed. Sample HA1 is a hematite concretion from Jerrinah, southwest of Wittenoom, WA. Sample HA2 is a hematite iron ore from middle Precambrian rocks of the Animikie Group, Marquette Iron Range, Ishpeming, Michigan, USA. Pigmentary hematite was also studied from so-called zebra rock (Abrajevitch et al., 2018), which has a striking rhythmic pattern produced by hydrothermally formed hematite with reddish-brown bands, rods, and elliptical spots of pigment and light background. Zebra rock occurs in thin discontinuous outcrops of stratified claystone from the Late Proterozoic Johnny Cake Shale, Ranford Formation, WA (Dow & Gemuts, 1969). Finally, a 5-mm crystal fragment of natural specularite from Mt Shimotoku, Okayama Prefecture, Japan, was studied from the collection of the Geological Museum, Geological Survey of Japan (Registration number A31-36426). Hematite crystals from this locality contain Mn, Si, Mg, and Cu impurities (at <0.1 wt % levels; Iwata, 1965).

4. Methods

Most of our FORC measurements were made with a Princeton Measurements Corporation vibrating sample magnetometer (VSM) at the Australian National University (ANU). Measurements were made either with the regular grid protocol of Pike et al. (1999) or the irregular grid protocol of Zhao et al. (2015) with measurements made at equal magnetization steps rather than equal field steps. Measurements generally take ~2 hr per sample with 200–250 ms averaging times and a 1 T maximum applied field; some samples saturate magnetically at 1 T and others do not. While presenting non-saturation results is not ideal, Roberts et al. (2006) argued that high-coercivity minerals are often analyzed using standard equipment with non-saturating fields, so such FORC measurements have comparative value. The more extensive FORC measurement types of Zhao et al. (2017) were made for representative samples to produce conventional FORC, remanence FORC (remFORC), induced FORC (iFORC), and transient FORC (tFORC) diagrams. It generally takes ~6 hr per sample for this suite of measurements. For red pigment samples with exceptionally high coercivities, more time-consuming FORC measurements were made at room temperature to (saturating) maximum fields of 5 T using a Quantum Design Magnetic Properties Measurement System (MPMS) at ANU. Conventional FORC measurements took 30 hr with this approach; the extended FORC measurement sequence took ~4 days because of the repeated large field sweeps from 0 to 5 T. FORC distributions were calculated with the xFORC software of Zhao et al. (2015).

High-temperature magnetic susceptibility (χ-T) was measured to rule out magnetite or maghemite impurities in natural samples and to assess potential cation substitutions. Measurements were made at a heating/cooling rate of 12°C/min in air using an AGICO Kappabridge MFK2 system with CS-4 oven at ANU. Zero-field-cooled (ZFC) and field-cooled (FC) M_{rs} were measured with the MPMS at ANU during warming from 5 to 300 K at ~2 K intervals. After cooling to 5 K in zero-field, a 5 T direct current (DC) field was applied and was then switched off to impart M_{rs}. M_{rs} curves were measured to 300 K at 1 K/min. FC-M_{rs} curves were measured by applying a 5 T DC field during cooling from RT to 5 K, switching the field off, and measuring M_{rs} to RT at 1 K/min.

Powder X-ray diffraction (XRD) analysis was carried out on a magnetic extract of sample LAN9 after grinding it in an agate mortar, stirring the powder into a slurry, and extracting magnetic particles with a rare Earth magnet within a plastic sheath. The extract was then mixed with ethanol and pipetted onto a low-background silicon holder and dried. Analyses were made with a Malvern Panalytical Empyrean Series 3 diffractometer equipped with Bragg-Brentano^{HD} divergent beam optics and a PIXcel^{3D} detector (1D scanning mode, 3.347° active length). Analysis was made using Co$K\alpha$ radiation over the 4–85° 2θ range, with 0.0131303° 2θ step width and 73 s/step dwell time, while spinning horizontally. Phases were identified with the DiffracPlus Eva 10 (2004) software and ICDD PDF-2 database (2004), and quantified with the Siroquant V4 software.

5. Results

5.1. Mineralogy of Hematite Samples

Transmission electron microscope (TEM) and scanning electron microscope (SEM) images of the studied samples are shown in Figure 3. Further XRD characterizations of synthetic samples are given in the original papers (see Section 3.1). Low-temperature ZFC/FC curves (Figure 4a) for a representative regolith sample (LAN9) have a clear Morin transition (Morin, 1950) at 240 K and no Verwey transition at 100–120 K (Verwey, 1939), which is consistent with the presence of pigmentary hematite nanoparticles and an absence of magnetite. The M_{rs} decrease during warming below T_M with higher values in the FC compared to the ZFC curve is similar to the results of Lagroix and Guyodo (2017) for a natural hematite in which a remanence was acquired during cooling in a 2.5 T field. We interpret the signal below T_M as a paramagnetic response due to kaolinite and/or anatase (Figure 4c) in a non-canceled residual field within the MPMS. A high-temperature χ-T curve for sample LAN9 (Figure 4b) has a Hopkinson peak at ~570°C that at first sight might be interpreted to indicate the presence of magnetite. However, χ decreases with heating to ~620°C, which is too high to be due to magnetite and could be due to cation-substituted hematite (e.g., Al; Jiang et al., 2021). The rest of the χ signal disappears at ~680°C and is associated with hematite. The broad unblocking temperature distribution and the break in slope at 620°C with final decrease to 680°C could indicate two hematite components. The χ-T curve is irreversible, with weaker χ during cooling. High-temperature treatment causes annealing and reduces the defect moment magnitude in hematite (Abrajevitch et al., 2018; Dunlop, 1971), which tends to be negligible in large unstrained hematite crystals but large in strained or otherwise imperfect particles (de Boer & Dekkers, 1998), including hematite nanoparticles (e.g., Dunlop, 1970, 1971, 1972; de Boer & Dekkers, 1998; Dekkers & Linssen, 1989; Nininger & Schroeer, 1978; Özdemir & Dunlop, 2014). The final χ value after annealing is severalfold lower than before heating (Figure 4b).

XRD results for magnetic minerals extracted from red-pigmented sample LAN9 (Figure 4c) indicate that it contains four minerals: quartz (33.2%), kaolinite (26.7%), anatase (11.9%), and hematite (28.2%). The extract consists of small rock fragments with pigmentary hematite rosettes (high backscatter in Figure 4d). Intergrown crystals with apparently random orientations and ~3–7 μm sizes (Figure 4e) co-occur with individual hematite crystals of similar size. XRD peaks for hematite are broad (Figure 4c). Best-fitting Rietveld (1969) refinements indicate two hematite components with the same abundance (14.1% each) but slight crystallinity differences (the (030) peak is split for the two hematite components (Figure 4c, inset); fitted peaks are for a rhombohedral cell with a = 5.0319 Å for hematite A and a = 5.0235 Å for hematite B). While our regolith samples appear to have random hematite orientations (Figure 4e), some sample types can have preferred particle orientations (e.g., red beds, iron ores) that could affect FORC comparisons among different sample types. Preferential hematite alignment may be detectable with low-temperature magnetic measurements (Abrajevitch et al., 2021).

Hematite is the only magnetic mineral detected in the studied synthetic and natural samples (Figures 3 and 4). Magnetite and/or maghemite impurities would significantly distort the magnetic properties of the samples,

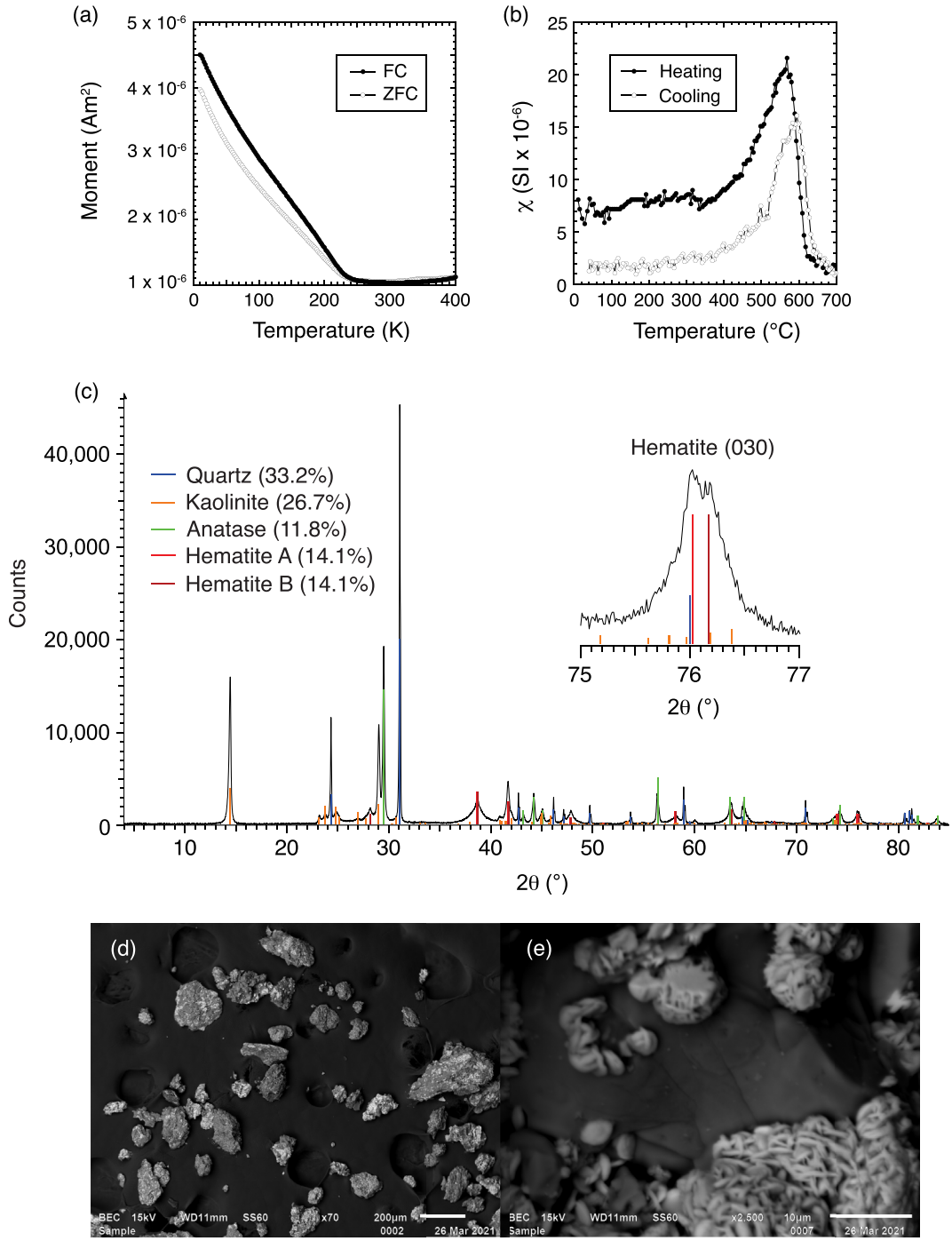

Figure 4. Mineral characterization of regolith sample LAN9. (a) Low-temperature field-cooled (FC) and zero-field cooled (ZFC) curves for a room-temperature M_{rs} imparted in a 5-T field. (b) χ-T curve. (c) XRD spectrum (Co$K\alpha$ radiation) for a magnetic extract with Rietveld (1969) refinement. Hematite peaks are broad and split; fitting two hematite components (A) and (B) produces an optimal fit (inset: (030) reflections). Identified mineral peaks are indicated. (d, e) SEM images of (d) rock fragments from the extract; bright backscatter is hematite pigment (200 μm scale bar), and (e) close-up of intergrown pigmentary hematite rosettes with ~3–7 μm plates (10 μm scale bar).

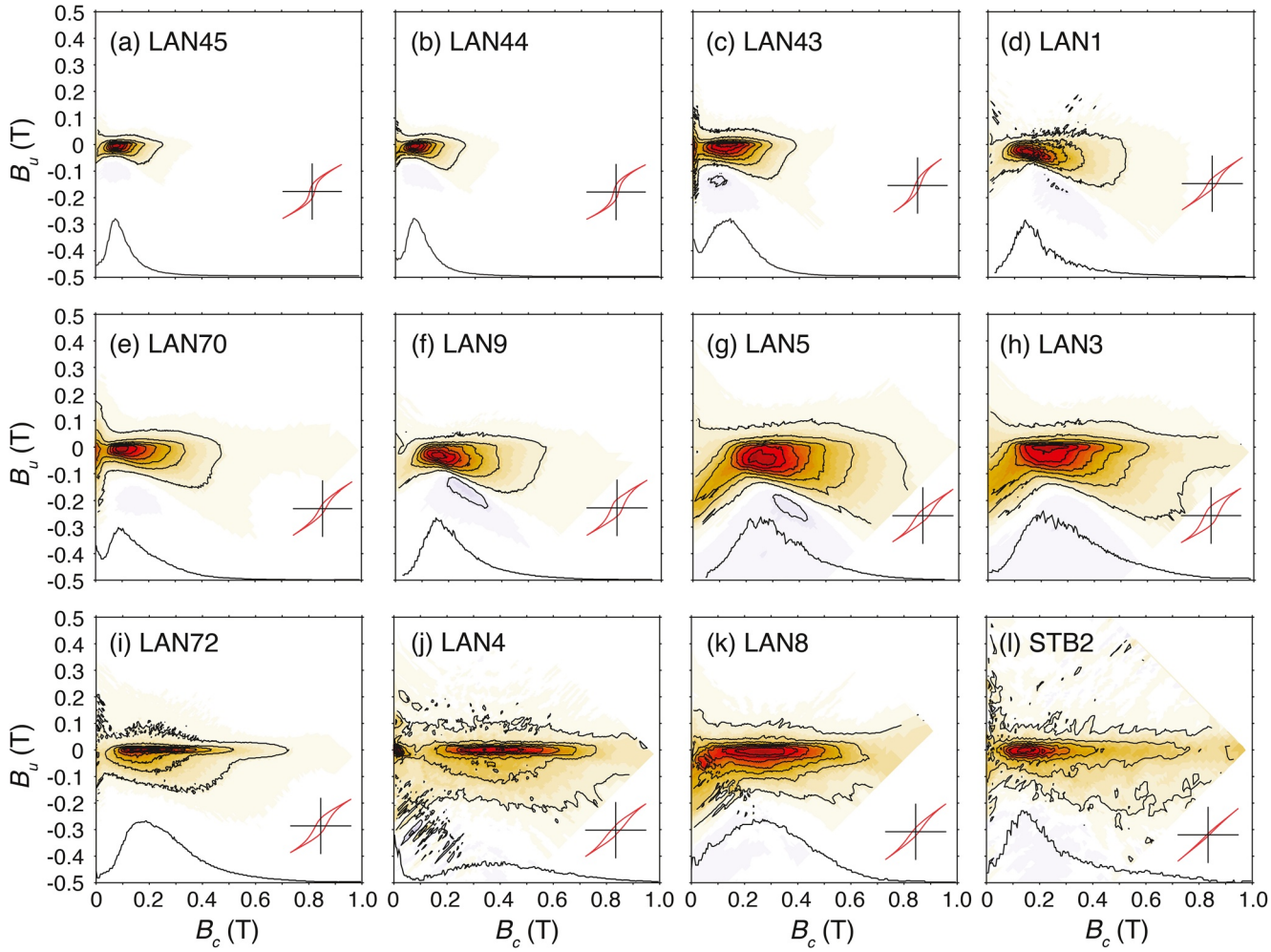

Figure 5. FORC diagrams for natural hematite samples with variable coercivity distributions from regolith, Yilgarn Craton, Western Australia. Samples are shown with progression from lower to higher coercivity for kidney-shaped FORC distributions: (a) LAN45, (b) LAN44, (c) LAN43, (d) LAN1, (e) LAN70, (f) LAN9, and (g) LAN5. Samples with mixed kidney-shaped and ridge-type FORC diagrams are shown in: (h) LAN3, (i) LAN72, (j) LAN 4, (k) LAN 8, and (l) STB2. Uncorrected major hysteresis loops are shown for ±1 T peak fields in the lower right-hand side and B_c profiles through the peak of each FORC distribution are shown at the bottom of each FORC diagram. SF = 3 and t_{avg} = 200 ms for all FORC diagrams, which were measured using the irregular grid protocol of Zhao et al. (2015).

including the FORC diagrams presented here in which they would be immediately detectable. Their presence even in trace amounts is excluded by these data.

5.2. FORC Results for Hematite Samples

Two main FORC diagram types are observed here. FORC distributions with "kidney", "banana", or "boomerang" shapes (e.g., Figures 5a–5h) are reported widely for natural hematite (e.g., Brownlee et al., 2011; Carvallo & Muxworthy, 2006; Carvallo et al., 2006; Church et al., 2016; Jovane et al., 2011; Liu et al., 2010; Martín-Hernández & Guerrero-Suárez, 2012; Muxworthy et al., 2005; Zhao et al., 2017). The kidney-shaped feature is an asymmetrical closed structure with variable coercivities from which two positive diagonal wings depart at ±45°, with a negative region below the main peak with slope at −45° away from the peak. Most, and sometimes all, of this kidney-shaped structure lies below $B_u = 0$. A second FORC distribution type for hematite samples has a dominant symmetrical, sharper, "ridge-type" signal (e.g., Figures 5i–5l) that is typical of uniaxial SD particle assemblages (e.g., Egli et al., 2010). Ridge-type FORC distributions have been observed widely for synthetic (Figures 6c, 6g–6i) (e.g., Jiang et al., 2016; Pariona et al., 2016; Roberts et al., 2006) and natural (Figures 7a and 8a) hematite nanoparticle assemblages. Negative regions expected along the lower B_u axis for uniaxial SD particle systems (e.g., Muxworthy et al., 2004; Newell, 2005) are not always evident in these conventional FORC

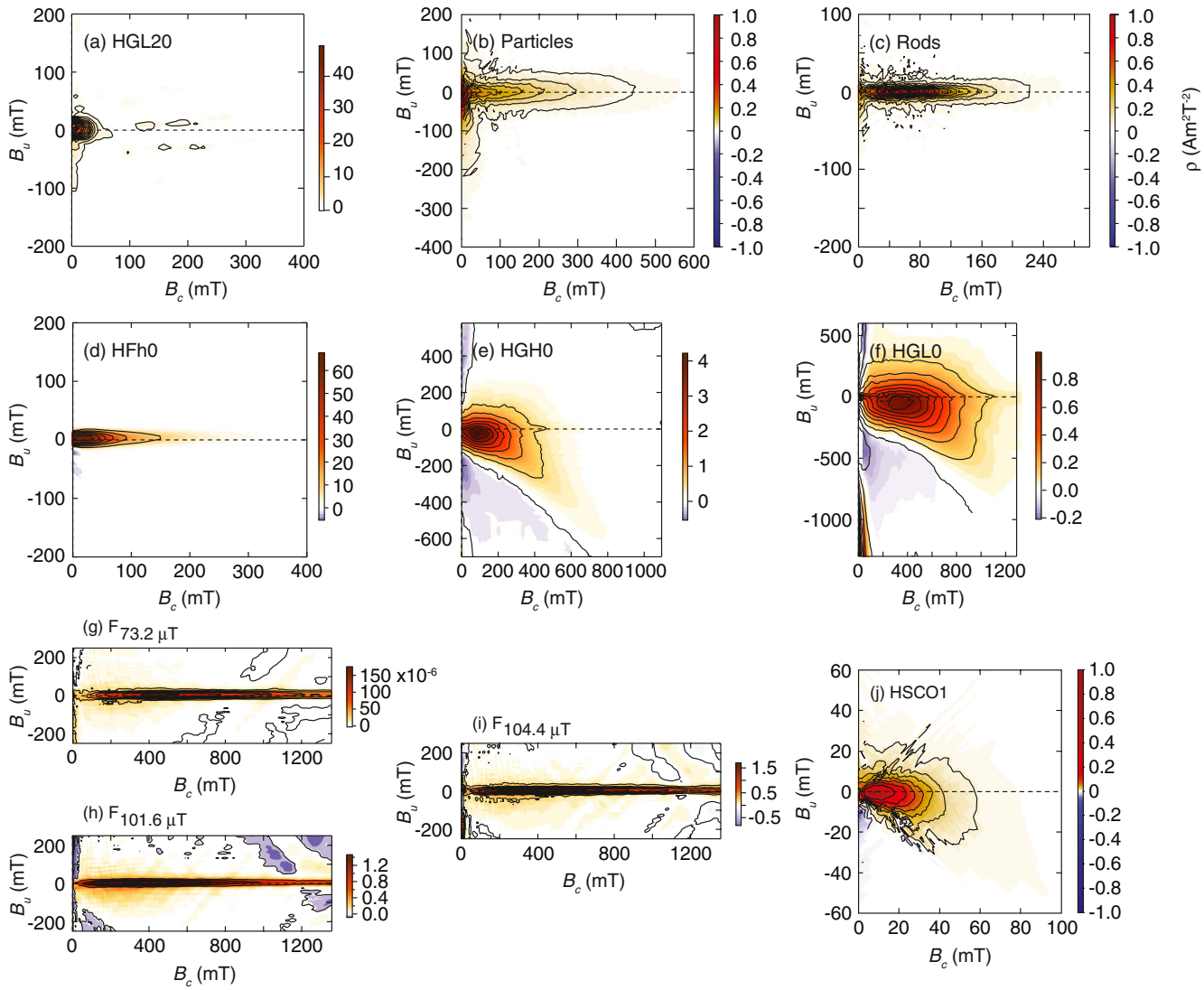

Figure 6. FORC diagrams for synthetic hematite powder samples. Results are shown for samples: (a) HGL20 from Jiang et al. (2012), (b) particle and (c) rod morphologies from Chen and Lin (2014), (d) HFh0, (e) HGH0, and (f) HGL0 from Jiang et al. (2012), (g) $F_{73.2\ \mu T}$, (h) $F_{101.6\ \mu T}$, and (i) $F_{104.4\ \mu T}$ from Jiang et al. (2016). (j) Coarse synthetic hematite (Figures 3h and 3i) for sample HSCO1 synthesized here. Samples were measured with the regular grid of Pike et al. (1999) and data were processed with either a fixed smoothing factor (SF) or VARIFORC smoothing (Egli, 2013; Harrison & Feinberg, 2008) as follows: (a) $s_{c,0} = 4$, $s_{c,1} = 4$, $s_{b,0} = 4$, $s_{b,1} = 4$, $\lambda_c = 0.15$, $\lambda_b = 0.15$, (b, c) SF = 3, (d) $s_{c,0} = 4$, $s_{c,1} = 4$, $s_{b,0} = 4$, $s_{b,1} = 4$, $\lambda_c = 0.1$, $\lambda_b = 0.1$, (e) $s_{c,0} = 6$, $s_{c,1} = 8$, $s_{b,0} = 6$, $s_{b,1} = 8$, $\lambda_c = 0.1$, $\lambda_b = 0.1$, (f) $s_{c,0} = 6$, $s_{c,1} = 8$, $s_{b,0} = 6$, $s_{b,1} = 8$, $\lambda_c = 0.1$, $\lambda_b = 0.1$, (g) $s_{c,0} = 6$, $s_{c,1} = 8$, $s_{b,0} = 6$, $s_{b,1} = 8$, $\lambda_c = 0.1$, $\lambda_b = 0.1$, (h) $s_{c,0} = 5$, $s_{c,1} = 7$, $s_{b,0} = 5$, $s_{b,1} = 7$, $\lambda_c = 0.1$, $\lambda_b = 0.1$, (i) $s_{c,0} = 5$, $s_{c,1} = 7$, $s_{b,0} = 5$, $s_{b,1} = 7$, $\lambda_c = 0.1$, $\lambda_b = 0.1$, and (j) SF = 2.

diagrams because of overlap with other positive contributions, although they are present in iFORC diagrams (Figures 7e, 7f and 8d, 8h). Mixtures between the two FORC distribution types are also observed (Figures 5i–5l), particularly in natural iron ores that contain more than one hematite component (Figure 7).

Major hysteresis loops are shown with each FORC diagram in Figures 2, 5, 7 and 8. While some loops are saturated at 1 T maximum applied fields, others are not. In particular, the zebra rock is far from saturation at 1 T (Figures 8a and 8b), and does not reach saturation until ~2 T (Figure 8f) (Abrajevitch et al., 2018). FORC measurements were made to 1 and 5 T maximum fields, respectively, for a red zebra rock sample to compare partial and full FORC distributions for the high coercivity hematite pigment in these samples (Figures 8b and 8f). A typical FORC distribution is well-defined with 120 FORCs (Figure 8a). For more time-consuming MPMS measurements, we measured 80 FORCs. VSM measurements with 80 FORCs (Figure 8b) have lower resolution

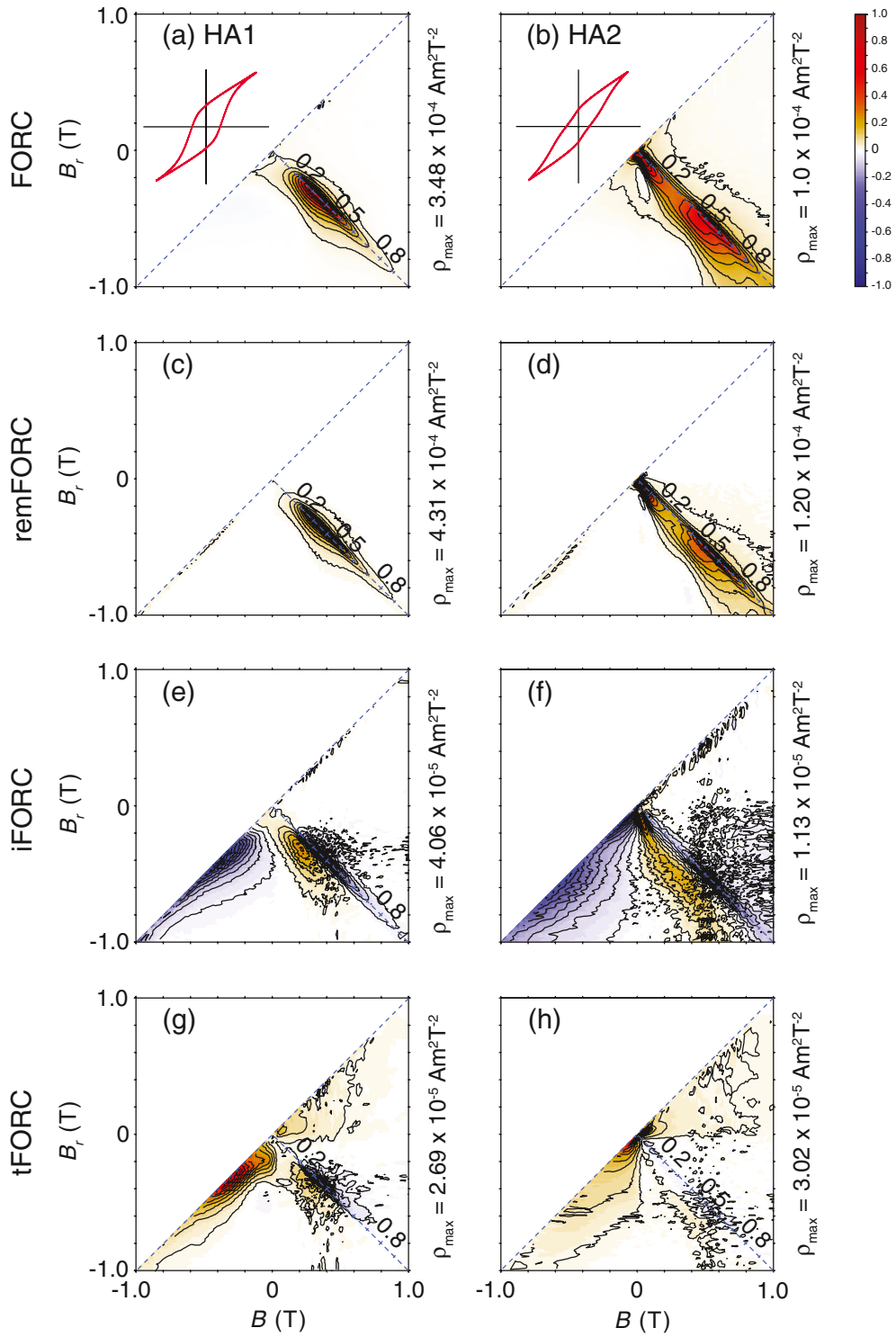

Figure 7. FORC diagrams for iron ore samples. Conventional FORC, remFORC, iFORC, and tFORC diagrams, respectively, for samples (a, c, e, g) HA1 and (b, d, f, h) HA2. See Section 3 for sample descriptions. Sample HA2 has two hematite components.

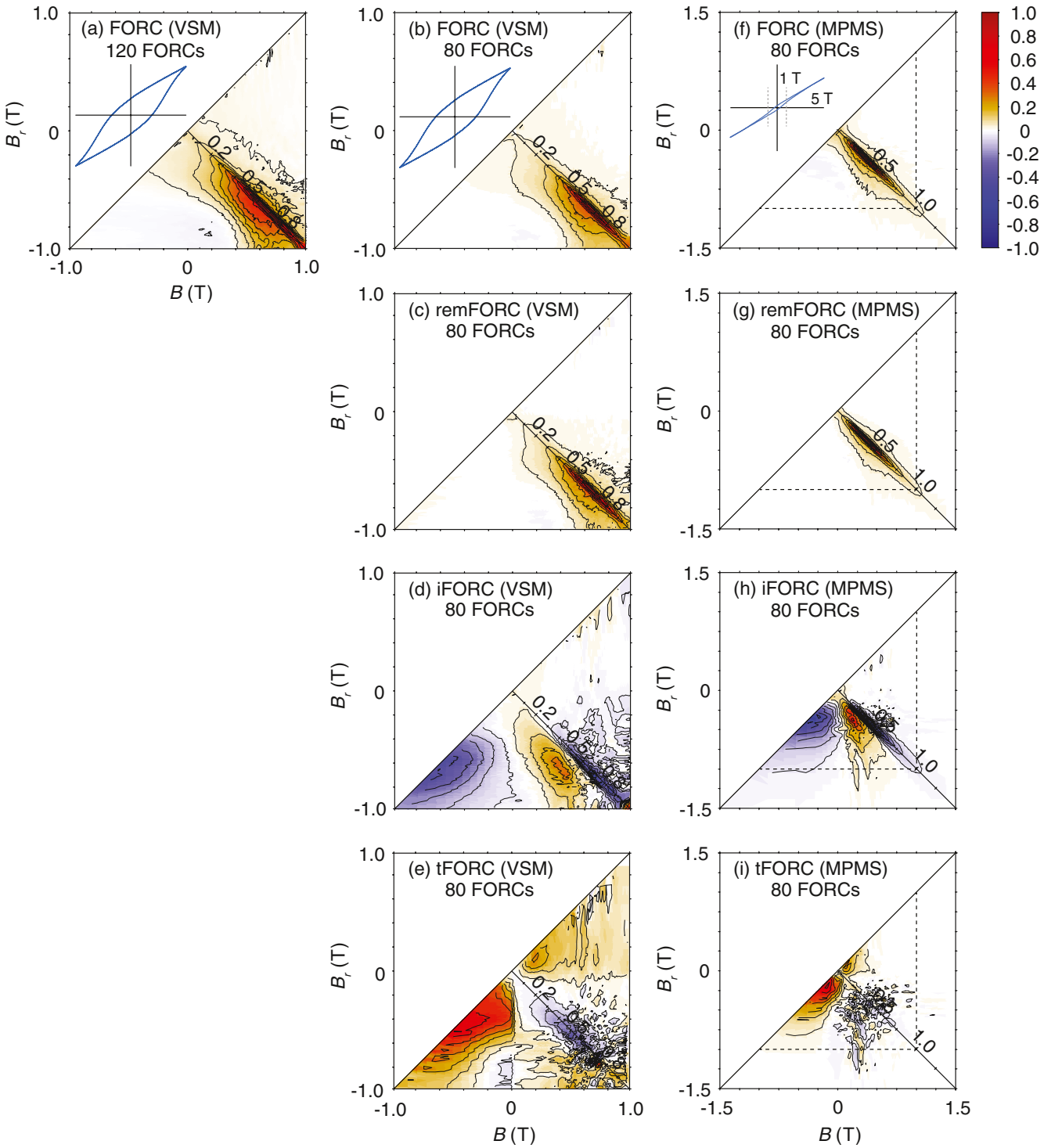

Figure 8. Comparison of FORC diagrams measured to 1 T and 5 T maximum fields to compare the saturation and non-saturation magnetic properties of the high-coercivity red zebra rock of Abrajevitch et al. (2018). (a) Measurement to 1 T with 120 FORCs compared with (b) measurement to 1 T with 80 FORCs, and (f) measurement to 5 T with 80 FORCs. Also shown are (c) remFORC, (d) iFORC, and (e) tFORC diagrams from measurements made to 1 T and (g) remFORC, (h) iFORC, and (i) tFORC diagrams from measurements made to 5 T.

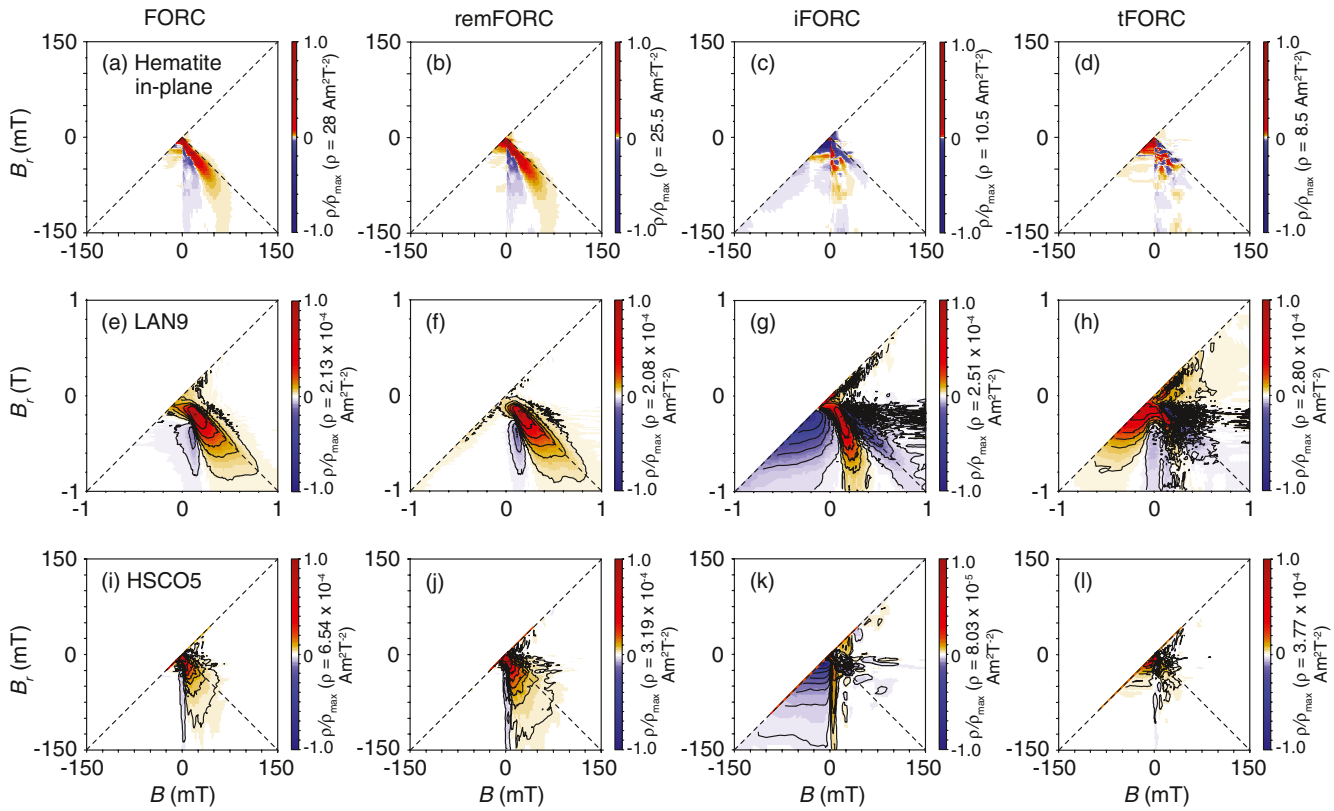

Figure 9. Conventional FORC, remFORC, iFORC, and tFORC diagrams for (a–d) a 5-mm hematite crystal (in-plane), (e–h) LAN9, and (i–l) HSCO5; (a) is similar to Figure 2g and was measured with a smaller field step of ~0.1 mT and slow slew rate to minimize overshoots. Measurement orientation was unconstrained compared to Figure 2g.

than for 120 FORCs (Figure 8a), although the main features are still captured. MPMS measurements with a 5 T maximum field (Figure 8f) capture the complete FORC distribution.

Diverse FORC distributions are observed for synthetic hematite samples. Sample HGL20 has a particle size of 32 ± 7 nm with 15.8 mol. % Al (Jiang et al., 2012). The exceptionally low coercivity in the FORC diagram for these hematite nanoparticles (Figure 6a) is indicative of a particle size around and just above the SP/SD threshold size, which is 17 nm for Al-hematite (Jiang et al., 2014). Such low coercivities are normally associated with ferrimagnetic minerals such as magnetite or maghemite, but they are also fundamental to hematite nanoparticles near the SD blocking volume (e.g., Jiang et al., 2012, 2014; Pike et al., 2001; Özdemir & Dunlop, 2014; Roberts et al., 2020). The vertical part of the FORC distribution along the lower B_u axis in Figure 6a also indicates that sample HGL20 contains magnetically viscous particles near the SP/SD threshold size (Pike et al., 2001). Slightly coarser 45–85 nm stoichiometric hematite particles have distributed coercivities (Figure 6b) that overlap the coercivity range of sample HGL20, with a vertical distribution along the lower B_u axis that is indicative of thermal activation of particles near the SP/SD threshold size, along with stable SD properties that have coercivities up to >500 mT. The remaining synthetic hematite samples have higher coercivities, as expected for hematite, with both ridge-type (Figures 6b–6d and 6g–6i) and kidney-shaped (Figures 6e, 6f, 6j) distributions.

The iron ore (Figure 7) and zebra rock (Figure 8) samples have mixed kidney-shaped and ridge-type FORC distributions with high coercivities. The Marquette iron ore has two hematite components: a kidney-shaped distribution with coercivities up to 200 mT and a mixed high coercivity kidney-shaped/ridge-type distribution (Figure 7b). These two FORC diagram types for hematite are discussed below and are illustrated by single crystal measurements (Figure 2).

Conventional FORC diagrams (Figures 2, 5 and 6), and remFORC, iFORC, and tFORC diagrams (Zhao et al., 2017) are shown for representative samples (Figures 7–9). These extensive results (Figures 2, 5–9) illustrate the range of FORC diagrams observed for natural and synthetic hematite samples. The origins of the two

observed FORC distribution types for hematite and the signatures associated with domain state variations in hematite are discussed below, along with diagnostic information from remFORC, iFORC, and tFORC diagrams (Zhao et al., 2017).

6. Discussion

6.1. FORC Signatures of Uniaxial and Triaxial Magnetocrystalline Anisotropy in Hematite

We document two FORC distribution types for hematite particles ("kidney-shaped" and "ridge-type"). It is important to understand the controls on these contrasting FORC signatures when interpreting experimental FORC results. Ridge-type signatures are readily explained as a manifestation of uniaxial SD magnetic behavior (Egli et al., 2010; Muxworthy et al., 2004; Newell, 2005; Pike et al., 1999). Kidney-shaped FORC distributions are less well explained and have also been observed in monoclinic 4C (Horng, 2018; Wehland et al., 2005) and authigenic pyrrhotite (Horng, 2018; Kars & Kodama, 2015a, b; Larrasoaña et al., 2007; Roberts et al., 2010; Weaver et al., 2002), which is a ferrimagnetic hexagonal 3C pyrrhotite (Horng & Roberts, 2018). Roberts et al. (2010) attributed the similar kidney-shaped features for hematite and pyrrhotite to the fact that their spontaneous magnetizations are confined to the basal crystallographic plane. Harrison et al. (2019) varied the balance between uniaxial and triaxial (hexagonal) anisotropies to simulate and explain the observed ridge-type and kidney-shaped FORC distributions for hematite.

Harrison and Lascu (2014) demonstrated that a negative region with slope at −45° away from the main peak is characteristic of FORC distributions for particle systems controlled by cubic anisotropy. This finding has been confirmed in numerical FORC simulations of randomly oriented particles with cubic anisotropy (Egli, 2021; Valdez-Grijalva & Muxworthy, 2019). Harrison et al. (2019) used the micromagnetic FORCulator tool of Harrison and Lascu (2014) to simulate FORC diagrams for magnetostatically interacting and noninteracting SD particles. Such simulations enable experimental FORC calibration by specifying the basic physical properties of a magnetic particle assemblage, including the number, volume, and M_s of particles, and statistical properties, including the spatial arrangement, type and orientation of anisotropy axes, and switching field distribution type. Harrison et al. (2019) restricted their triaxial anisotropy simulations to noninteracting cases with randomly oriented particles. For low uniaxial to triaxial anisotropy ratios, $|K_1/K_3|$ (see Equation 1), which allows magnetic moments to lie outside the basal plane (see Figure 10 caption for explanation), simulated FORC diagrams are dominantly of uniaxial type with a sharp ridge in both FORC (Figure 10a) and remFORC diagrams (Figure 10b). The iFORC diagram has a negative-positive-negative (N-P-N) signature (Figure 10c) that is typical of SD behavior (Harrison et al., 2019; Zhao et al., 2017). The tFORC diagram has no signal (only numerical noise) because noninteracting SD particles do not produce a transient hysteretic response (Fabian, 2003; Harrison et al., 2019; Zhao et al., 2017). In contrast, high $|K_1/K_3|$ values constrain moments to lie within the basal plane, which produces more complex asymmetric FORC and remFORC diagrams (Figures 10e and 10f), and even more complex iFORC diagrams (Figure 10g). Thus, a transition from triaxial to uniaxial magnetization switching occurs at a critical value of the out-of-plane/in-plane anisotropy ratio and asymmetric FORC distributions obtained for triaxial anisotropy are explained by the availability of multiple basal plane easy axes. Further FORC simulations for an anisotropy (particle size/coercivity) distribution (Figure 10i) with moments constrained to lie within the basal plane (i.e., high $|K_1/K_3|$) contain features (Figure 10j) that are more representative of natural kidney-shaped distributions (Figures 5a–5h). The sharp positive and negative ridges with −45° slope that are present for a single anisotropy value (Figure 10e) merge into more diffuse positive and negative regions below the central ridge in Figure 10j. This vertical FORC distribution blurring is due to addition of multiple distributions as seen in Figure 10e along the horizontal axis. The simulation in Figure 10j is for a noninteracting SD case, so the vertical blurring cannot be due to magnetostatic interactions.

Despite limitations due to the number of particles that can be simulated, consistency between simulated and experimental FORC diagrams for hematite demonstrates that kidney-shaped FORC diagrams for hematite are due to its triaxial basal plane anisotropy. The value of FORC diagrams is generally considered to lie in diagnosing domain state, and in providing measures of the coercivity and magnetostatic interaction field distributions of samples (e.g., Roberts et al., 2000, 2014). As demonstrated in several studies (e.g., Egli, 2021; Harrison et al., 2019; Harrison & Lascu, 2014; Valdez-Grijalva et al., 2018; Valdez-Grijalva & Muxworthy, 2019), FORC diagrams also contain rich information about magnetocrystalline anisotropy type that is linked directly to mineralogy. This adds an important level of diagnostic information available from FORC diagrams.

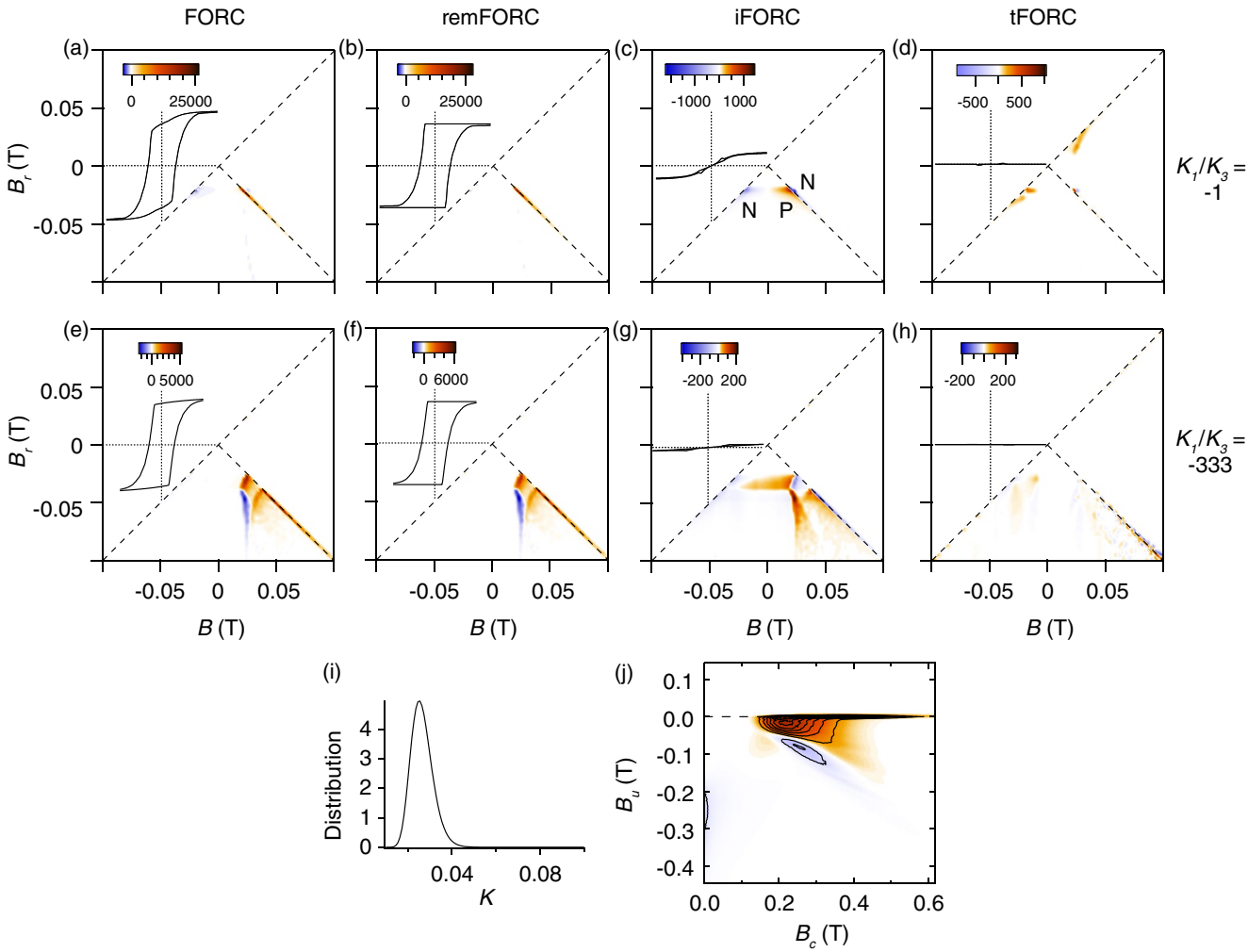

Figure 10. FORC simulations (Harrison et al., 2019) for magnetically noninteracting particles with uniaxial or triaxial (hexagonal) anisotropy that constrain FORC diagram interpretation for hematite. Simulated (a, e) FORC, (b, f) remFORC, (c, g) iFORC, and (d, h) tFORC diagrams for cases where (a–d) uniaxial behavior dominates (i.e., $K_1/K_3 = -1$) and where (e–h) triaxial behavior dominates (i.e., $K_1/K_3 = -333$). A sharp central ridge dominates the (a, b) FORC and remFORC diagrams, the (c) iFORC diagram has a dominant negative-positive-negative (N-P-N) signal, and (d) the tFORC diagram has only numerical noise; these properties are representative of noninteracting uniaxial SD systems (Harrison et al., 2019; Zhao et al., 2017). More complex features are observed for triaxial anisotropy (see Harrison et al. (2019) for details). When K_1 is large and negative (i.e., $|K_1| >> |K_3|$), spins are constrained strictly within the basal plane; spins cannot rotate out of plane, so they must rotate within the plane and are exposed to the full effect of K_3. Dominant K_1, thus, forces the material to behave in the most "triaxial" manner. When $|K_1| = |K_3|$, the uniaxial component is much weaker, so spins can rotate out, with less triaxial in-plane influence to produce more "uniaxial" behavior. Simulations for (i) distributed K (i.e., K_1 and K_3 vary through a range of values while keeping K_1/K_3 fixed at $K_1/K_3 = -333$) yield a (j) conventional FORC diagram with features similar to those observed in natural hematite pigment samples (e.g., Figure 5 [see text]).

Uniaxial shape anisotropy dominates cubic magnetocrystalline anisotropy in magnetite even for only slightly elongated particles (e.g., Tauxe et al., 2010). This is not so for hematite, which has weak M_s. "Uniaxial-type" FORC signatures are observed (Figure 6b) for roughly equidimensional synthetic hematite particles (Figure 3f), so ridge signals do not result from particle elongation. Magnetostrictive anisotropy associated with uniaxial internal stresses (see Section 2.3) control the coercivity of hematite (Banerjee, 1963; Mizushima & Iida, 1966; Porath & Raleigh, 1967; Porath, 1968; Stacey & Banerjee, 1974; Sunagawa & Flanders, 1965), and are enhanced in nanoparticles (Bruzzone & Ingalls, 1983; Muench et al., 1985; Nininger & Schroeer, 1978; Searle, 1967). We interpret ridge-type signals for hematite nanoparticles to reflect a stress-induced uniaxial anisotropy (K_u in Equation 1) that dominates the intrinsic magnetocrystalline anisotropy. While Harrison et al. (2019) simulated signals associated with uniaxial magnetocrystalline anisotropy (K_1 in Equation 1), it is expected that K_u is dominant in SD systems and will produce equivalent uniaxial-type FORC diagrams. Thus, FORC diagrams reflect the balance between switching via coherent rotation of basal plane moments, along up to six easy axes (e.g., Figures 5a–5h),

or by uniaxial out-of-plane coherent rotation through the *c*-axis or by switching of stress-controlled moments (e.g., Figures 5i–5l, and 6g–6i). Signals due to both anisotropy types are observed experimentally (Figures 2, 5–9), even within the same sample, which suggests that hematite samples lie close to a critical boundary where factors such as shape, twinning, or stress may tip the overall magnetic behavior one way or the other (Harrison et al., 2019) or they contain two particle types with distinct switching mechanisms in each type. Triaxial basal plane anisotropy is demonstrated by periodic ($\sin^2(3\theta)$) M_{rs}, B_c, and B_{cr} variations in the basal plane of a 5-mm crystal (Figures 2a–2c), whereas perpendicular to the basal plane, these parameters indicate uniaxial ($\sin^2\theta$) anisotropy (Figures 2d–2f).

6.2. FORC Diagrams and Domain State Diagnosis in Hematite

In addition to providing information about the magnetic anisotropy type and its influence on magnetization switching, FORC diagrams are used to diagnose domain states in magnetic particle assemblages. We discuss here the FORC manifestations for domain states in hematite, which include domain state diagnostic information from remFORC, tFORC, and iFORC diagrams (Zhao et al., 2017) for which Harrison et al. (2019) provided explanatory simulations.

6.2.1. Superparamagnetic State

The FORC diagrams in Figures 6a and 6b are indicative of particles that span the SP/SD threshold. Such magnetically viscous hematite particles are common in nature (e.g., Collinson, 1969; Creer, 1961; Jiang et al., 2015; Pike et al., 2001; Stokking & Tauxe, 1990), along with stable SD particles (e.g., Figures 5c and 5e). The FORC manifestations of thermal activation associated with such particles are explained by Pike et al., (2001); the key manifestation is an asymmetrical positive feature near the origin, with a dominantly vertical distribution along the lower B_u axis and a small response in the upper FORC half-plane (see also Berndt et al., 2018 and Egli, 2021).

6.2.2. Stable Single Domain State

Detrital sediment particles tend to have sizes in the tens of microns range, while authigenic hematite pigments have sizes from tens of nanometers to microns (e.g., Figures 3 and 4e). Natural hematite with these sizes is likely to be in the stable SD state (Banerjee, 1971; Jiang et al., 2014; Kletetschka & Wasilewski, 2002; Özdemir & Dunlop, 2014), as indicated by dominantly concentric FORC contours for natural (Figures 5, 7 and 8) and synthetic (Figure 6) samples. Large negative-positive-negative (N-P-N) iFORC signals (Figures 7e, 7f, 8d, 8h, and 9g) confirm the SD dominance, and are consistent with simulations for uniaxial noninteracting SD hematite (Figure 10c; Harrison et al., 2019). The complex iFORC signals in triaxial anisotropy simulations (Figure 10g) are only observed here within the basal plane of a 5-mm crystal (Figure 9c). The complex signal in Figure 9c is noisy, but features are as documented by Harrison et al. (2019) for noninteracting SD particles (Figure 10g). SD-like iFORC results for the crystal are consistent with its small MD signal (see below). Our FORC results indicate dominant SD behavior in natural hematite samples.

6.2.3. Is There a Vortex State in Hematite?

Non-zero tFORC signals reflect non-SD behavior (Fabian, 2003; Zhao et al., 2017) in iron ore (Figures 7g and 7h), zebra rock (Figures 8e and 8i), regolith (Figure 9h), coarse synthetic particles (Figure 9l), and a 5-mm crystal (Figure 9d). This raises questions about the nature of non-SD states and whether vortex structures exist in hematite. Magnetic particles develop magnetization configurations that minimize the total free energy E_{tot}, which is the sum of the exchange, anisotropy (Equation 1), magnetostatic, magnetostrictive (or magnetoelastic) strain, and demagnetization (E_d) energies (e.g., Coey, 2010). E_d increases with particle size because it scales with M_s^2 and volume scales with the cube of particle length in equidimensional particles. As particles approach a critical size, E_d dominates and non-uniform magnetic states develop to eliminate surface poles and stray fields. In soft ferrimagnets, uniform SD magnetizations diverge into a flower state with increasing particle size, above which a single vortex (SV) nucleates to minimize E_{tot} (Schabes & Bertram, 1988; Williams & Dunlop, 1989). In hard magnetic materials, the most favorable flux-closure configuration can involve a direct transition from the SD to MD state (Kittel, 1949).

Two micromagnetic parameters can help to assess whether an intermediate SV state exists in hematite or if a MD state develops directly. The dimensionless magnetic hardness parameter is:

$$\kappa = \sqrt{|K|/\mu_0 M_s^2} \tag{2}$$

and the exchange length is:

$$l_{ex} = \sqrt{A/\mu_0 M_s^2}, \tag{3}$$

where A is the magnetic exchange constant and μ_0 is the permeability of free space; l_{ex} is the shortest length scale on which the magnetization can change in response to dipolar fields. Magnetically hard materials have $\kappa > 1$ and soft materials have $\kappa < 1$ (Coey, 2010). If the largest particle that undergoes magnetization reversal via the curling mode (i.e., via SV formation, d_{SV}) is smaller than the domain wall thickness (δ_w), a SV state will form because the particle is too large to be homogeneously magnetized, but too small to host a domain wall. Conversely, if $d_{SV} > \delta_w$ a MD state forms directly when sufficient particle volume exists to accommodate a domain wall. For a 180° Bloch wall, $\delta_w = \pi\sqrt{A/K}$, which, from the above relations, can be expressed as (Coey, 2010):

$$\delta_w = \pi l_{ex}/\kappa \tag{4}$$

and the maximum SV particle size can be expressed as:

$$d_{SV} \approx 36\kappa l_{ex} \tag{5}$$

The largest SD particle that reverses its magnetization via coherent rotation in an applied field is:

$$d_{\mathrm{coh}} \approx \sqrt{24} l_{ex} \tag{6}$$

As a rough guide to vortex formation, we can consider the magnitudes of d_{coh} and δ_w. If $d_{coh} \geq \delta_w$, then vortices are unlikely to form during magnetization reversal. Using Equations 4 and 6 in this inequality ($\sqrt{24} l_{\mathrm{ex}} \geq \pi l_{ex}/\kappa$) gives $\kappa \geq \pi/\sqrt{24} \approx 0.64$, so vortices will not form when $\kappa \geq 0.64$. The $d_{SV} < \delta_w$ condition for direct transition to a MD state gives a lower limit for vortex formation from Equations 4 and 5 ($36\kappa l_{\mathrm{ex}} < \pi l_{ex}/\kappa$): $\kappa < \sqrt{\pi/36} \approx 0.3$. Thus, a SV state will exist for a given particle size range when $\kappa < 0.3$. Using $K = -1.35 \times 10^4$ Jm^{-3} (Fletcher & O'Reilly, 1974) and $M_s = 480$ kAm^{-1} for magnetite in Equation 2 gives $\kappa = 0.003$. Its magnetic softness means that magnetite particles between d_{coh} and d_{SV} contain vortices before a MD state is reached at larger sizes. For hematite, $K_3 = 0.7$–18.8 Jm^{-3} (Flanders & Schuele, 1964; Martín-Hernández & Guerrero-Suárez, 2012). Using $K = 0.7$ and 18.8 Jm^{-3}, $\mu_0 = 4\pi \times 10^{-7}$ Hm^{-1}, and $M_s = 2500$ Am^{-1} for hematite (Dunlop, 1971) in Equation 2 yields $\kappa = 0.3$ and 1.55, respectively. Thus, for intermediate to high K_3 values, hematite is too hard magnetically to allow SV formation, although vortices can exist in the remanent state when K_3 is low enough for $\kappa < 0.64$. Based on these considerations, we conclude that our tFORC signals are due to MD behavior; remanent vortex states should be rare in hematite. Vortex behavior reported in a hematite thin film (Chmiel et al., 2018) is not comparable to natural hematite because nanomagnetic properties are often manipulated in materials science applications.

Values of the magnetocrystalline anisotropy constants K_1 and K_3 for hematite cannot explain its coercivity (Banerjee, 1971; Dunlop, 1971). Coercivities of hundreds of mT for SD hematite require much higher K_u values (e.g., 1.53×10^3 Jm^{-3}) that are due to magnetostriction. Using $K_{hys} = B_c M_s/2$ (Cullity, 1972), most of our synthetic SD hematite samples have high anisotropy values of between hundreds and thousands of Jm^{-3} (Table 2), as expected.

6.2.4. Multidomain State

Given that vortex behavior is unlikely in hematite, our tFORC results are indicative of MD behavior (Figures 7–9). We analyzed three coarse hematite samples: synthetic samples HSCO1 and HSCO5 (~10–30 and ~100 μm; Figures 6j, 9i–9l) and a natural 5-mm crystal (Figures 2g, 2h, 9a–9d). Although noisy, these FORC distributions mainly have low coercivity; higher coercivities are present, but they are smaller than for natural and synthetic SD particles. FORC diagrams for the 5-mm hematite crystal are similar to a published in-plane FORC diagram for a natural crystal (Martín-Hernández & Guerrero-Suárez, 2012). A high coercivity portion for the 5-mm crystal fragment (Figures 2g, 2h and 9a, 9b) suggests that it is polycrystalline with SD regions. Low bulk B_c values of 15, 29, and 35 mT, respectively, for samples HSCO1, HSCO5, and A31-36426 (Table 2) are consistent with MD behavior (see B_c vs. particle size compilations of Özdemir and Dunlop, 2014 and Jiang et al., 2021). The threshold

Table 2
Hysteresis Parameters for the Studied Synthetic and Natural Hematite Samples

Sample	M_{rs} (Am^2 kg^{-1})	M_s (Am^2 kg^{-1})	B_c (mT)	B_{cr} (mT)	M_{rs}/M_s	B_{cr}/B_c	K_{hys} (Jm^{-3})
LAN45	6.26×10^{-2}	1.34×10^{-1}	97.8	129.8	0.47	1.33	
LAN44	6.31×10^{-2}	1.44×10^{-1}	96.7	135.0	0.44	1.40	
LAN43	2.57×10^{-2}	5.21×10^{-2}	121.4	179.3	0.49	1.48	
LAN1	4.31×10^{-3}	6.14×10^{-3}	242.3	285.0	0.70	1.18	
LAN70	6.13×10^{-2}	1.53×10^{-1}	193.7	362.8	0.40	1.87	
LAN9	7.81×10^{-3}	1.01×10^{-2}	257.1	287.2	0.78	1.12	
LAN5	1.35×10^{-2}	1.82×10^{-2}	340.4	386.4	0.74	1.14	
LAN3	1.32×10^{-2}	1.78×10^{-2}	305.0	352.1	0.74	1.15	
LAN72	1.49×10^{-2}	2.32×10^{-2}	256.1	330.5	0.64	1.29	
LAN4	1.70×10^{-3}	2.89×10^{-3}	349.8	496.0	0.59	1.42	
LAN8	2.13×10^{-3}	3.98×10^{-3}	256.0	376.9	0.53	1.47	
STB2	1.57×10^{-3}	3.22×10^{-3}	277.0	568.1	0.49	2.05	
HGL20	3.50×10^{-2}	1.21×10^{-1}	126.3	582.6	0.29	4.61	40
Particles	8.11×10^{-3}	2.24×10^{-2}	58.9	184.3	0.36	3.13	3.5
Rods	1.34×10^{-2}	2.76×10^{-2}	59.7	91.1	0.48	1.52	4.3
HFh0	9.76×10^{-2}	3.46×10^{-1}	33.5	78.7	0.28	2.35	31
HGH0	9.23×10^{-2}	1.88×10^{-1}	155.4	243.3	0.49	1.57	77
HGL0	1.50×10^{-1}	2.62×10^{-1}	370.8	504.0	0.57	1.36	255
$F_{73.2\ mT}$	1.62×10^{-1}	2.23×10^{-1}	705.7	958.7	0.72	1.36	414
$F_{101.6\ mT}$	1.80×10^{-1}	2.35×10^{-1}	467.9	611.1	0.77	1.31	2889
$F_{104.4\ mT}$	1.66×10^{-1}	2.24×10^{-1}	576.1	777.1	0.74	1.35	3395
HSCO1	6.39×10^{-3}	1.25×10^{-2}	14.6	20.8	0.51	1.42	0.5
HSCO5	9.02×10^{-4}	1.78×10^{-3}	29.2	50.0	0.51	1.71	0.1
HA1	9.61×10^{-2}	1.13×10^{-1}	362.8	383.5	0.85	1.06	
HA2	6.50×10^{-2}	9.17×10^{-2}	483.3	588.5	0.71	1.22	
Zebra red	7.58×10^{-2}	1.00×10^{-1}	645.3	725.1	0.76	1.12	
A31-36426 In-plane	4.64×10^{-2}	6.27×10^{-2}	34.8	45.0	0.74	1.30	5.7
A31-36426 Out-of-plane	6.19×10^{-4}	8.61×10^{-4}	173.7	213.7	0.72	1.23	0.4

Note. Hysteresis parameters were determined after high-field slope correction by fitting loops and extrapolating to saturation for samples that remained unsaturated at the maximum applied fields. Bulk anisotropy estimated from hysteresis parameters is: $K_{hys} = B_c M_s/2$ in units of T [$= kgs^{-2}\ A^{-1}] \times Am^{-1} = kgs^{-2}m^{-1} = Jm^{-3}$. For this calculation, M_s was converted from units of Am^2kg^{-1} to Am^{-1} by multiplying by the density of hematite (5,256 kgm^{-3}). K_{hys} values are only reported for synthetic and crystal fragment samples because hematite contents are unknown for the natural samples. K_{hys} values for our coarse samples are similar to those of Martín-Hernández and Guerrero-Suárez (2012) for single crystals, while large values for SD synthetic hematite are more consistent with those of Banerjee (1971).

size for the onset of MD behavior is debated (Özdemir & Dunlop, 2014). The high-coercivity FORC distribution for sample LAN9 (Figure 5f) indicates that its intergrown ~3–7 μm hematite plates (Figure 4e) fall within the SD size range. Sample HSCO5 has a particle size range up to ~100 μm, a low coercivity FORC distribution (Figure 9i), and low bulk B_c (Table 2), which suggest MD behavior. Importantly, it lacks the N-P-N iFORC signal (Figure 9k) that is indicative of SD behavior and it has a significant tFORC signal (Figure 9l) that indicates non-SD behavior. These results are consistent with a MD threshold size for hematite in the tens of microns range rather than ~100 μm as suggested by Kletetschka and Wasilewski (2002).

MD contributions can be quantified by integrating the tFORC response because transient hysteresis is produced by non-SD components (Fabian, 2003; Zhao et al., 2017). The upper half plane provides the best isolation of tFORC signals because induced magnetizations due to viscous particles near the SP/SD threshold size are smaller here than in the lower half plane. Integrated estimates are independent of FORC processing parameters (Egli

Table 3
Estimation of Non-SD FORC Contributions

Sample	Integrated FORC signal (Am^2)	Integrated tFORC signal (Am^2)	tFORC/FORC (%)
LAN9	1.04×10^{-5}	6.58×10^{-7}	6.3
HSCO5	5.20×10^{-7}	1.61×10^{-7}	31.0
HA1	1.98×10^{-5}	1.15×10^{-6}	5.8
HA2	1.54×10^{-5}	1.81×10^{-6}	11.8
Zebra red (MPMS)	2.60×10^{-3}	7.40×10^{-5}	2.8
A31-36426 (in-plane)	6.23×10^{-5}	7.78×10^{-7}	1.2

et al., 2010), which makes them valuable for non-SD signal quantification (e.g., Tauxe et al., 2021). We only have tFORC data for six samples: HA1, HA2 (Figure 7), zebra rock (Figure 8), and the three samples in Figure 9. These samples span the domain state spectrum for hematite, with signals due to viscous SP/SD, stable SD, and MD behavior. The non-SD contribution is estimated by integrating the upper half plane tFORC signal, doubling it to represent the entire tFORC signal, and dividing it by the total integrated FORC signal. The resulting tFORC/FORC signal (×100) represents the percentage non-SD contribution (Table 3), which we interpret to be due to MD particles. This interpretation is supported by the above discussion about the unlikely presence of vortex behavior in hematite and by the lack of lobe-like tFORC features (e.g., Roberts et al., 2017; Zhao et al., 2017) in the studied samples.

The zebra, HA1, and LAN9 samples have dominantly SD behavior with small (<6.3%) MD contributions (Figures 7–9; Table 3). Sample HSCO5 has the largest MD contribution (31%, Table 3). Perhaps surprisingly, the weakest tFORC signal is obtained for the 5-mm crystal (1.2%, Table 3), which was measured close to a basal plane easy axis (Figure 2a). High coercivity parts of Figures 2g, 2h and 9a, 9b are consistent with this polycrystalline fragment containing SD regions. Özdemir and Dunlop (2014) attributed widespread SD signals in hematite to its small internal demagnetizing field (<1 mT), which produces insignificant pressure to nucleate domain walls so that the remanence remains near saturation with high M_{rs}/M_s for MD particles. Resistance to domain wall nucleation is expected to control the hysteresis properties of hematite. Our approach is useful for quantifying MD hematite contents, although it will be challenging when soft ferrimagnetic minerals are present.

6.3. Are Interactions Responsible for Vertical Spreading in FORC Diagrams for Hematite?

Central ridge signatures in the studied hematite samples (e.g., Figures 6g–6i) indicate a lack of magnetostatic interactions (Egli et al., 2010; Pike et al., 1999) even though no precautions were taken to disperse synthetic particles. Central ridges are not sharp in this study because larger field spacings tend to be used compared to magnetite to define the high coercivities of hematite in FORC diagrams. B_u profiles through FORC distribution peaks can be used to compare interaction field distributions if the effective measurement resolution, which is a function of field spacing and vertical smoothing factor, is taken into account (Egli, 2021; Egli et al., 2010). Measurements were made here using variable field spacings (Zhao et al., 2015), which precludes such comparison. However, strong inter-particle interactions are not expected for hematite. The maximum interaction field will be $\approx \mu_0 M_s/2$ (i.e., 1.6 mT) near the pole of a point-source hematite particle, which is less than the field spacing in typical FORC measurements for hematite. Magnetostatic interactions are, therefore, unlikely to be resolved in FORC diagrams for hematite; if resolved, they will not contribute markedly to vertical spreading.

Multiaxial anisotropy produces more complex FORC distributions than uniaxial systems (Egli, 2021; Harrison et al., 2019; Valdez-Grijalva et al., 2018; Valdez-Grijalva & Muxworthy, 2019). For hematite, this means that the magnetization can switch through one of six directions along three basal plane easy axes. Thus, upward and downward hysteretic switching events can occur at different fields to produce complex FORC distributions (Figure 10e) compared to uniaxial cases (Figure 10a). Complex FORC responses for noninteracting SD particles with triaxial anisotropy (Figure 10e) indicate that vertical spreading is not only due to magnetostatic interactions. For noninteracting SD particles with distributed anisotropy (Figure 10i), horizontal and vertical features sum to produce greater vertical spread (Figure 10j) than in simulations for a single particle size (Figure 10e). The simulation in Figure 10j is similar to results for natural hematite (Figure 5), although some features are not captured. This illustrates the need to simulate FORC signatures to understand them using known magnetization processes. Available simulations make it clear that use of the Preisach (1935)-Néel (1954) coercivity-interaction framework to interpret horizontal and vertical FORC signals is inappropriate for particle systems with multiaxial anisotropy.

6.4. What Is the Cause of Vertical Spreading in the Upper FORC Half Plane?

Simulated FORC distributions are restricted to the lower FORC half plane (Figures 10e–10h, 10j) (Harrison et al., 2019), whereas experimental results also produce upper half plane responses (Figures 2, 5–9). This aspect of the FORC behavior of particle systems with multiaxial anisotropy is not well-explored. Part of the upper half plane response is due to unavoidable smoothing. For example, less smoothed simulated FORC distributions lie within the lower half plane, while more heavily smoothed distributions extend into the upper half plane (Valdez-Grijalva & Muxworthy, 2019). Inter-particle magnetostatic interactions are unlikely to cause spreading above $B_u = 0$ for hematite (Section 6.3). MD particles are responsible for some of the upper half plane signal (Section 6.2.4; Table 3). Thermally assisted switching or exchange interactions among intergrown or touching particles (e.g., Figure 4e) can also cause FORC distribution smearing into the upper half plane. For example, thermal activation can cause premature switching that leads to vertical spreading of FORC distributions above $B_u = 0$ (e.g., Berndt et al., 2018; Egli, 2006, 2021; Pike et al., 2001). Simulations with additional magnetization mechanisms are needed to understand the cause of spreading in the upper FORC half plane for particle systems with multiaxial anisotropy.

6.5. Saturation vs. Non-saturation Representations in FORC Diagrams?

Measurement to ~1 T maximum applied fields is often thought to be a major limitation of FORC diagrams for magnetic characterization of hematite-bearing samples. Roberts et al. (2006) argued that many magnetic techniques have similar limitations, which makes it important to characterize materials with widely used fields even if they represent non-saturation properties. This view is validated by results for a high-coercivity hematite pigment in zebra rock (Figures 8b and 8f). Although measurements to 1 T only capture part of the coercivity distribution (Figure 8b), with the full distribution captured in measurements to 5 T (Figure 8f), the two FORC distributions contain similar details below 1 T. Measurements to 1 T mainly miss information between 1 T and the saturating field. This confirms the value of measurements to 1 T with instruments used widely for FORC measurements. The major signatures due to hematite are identified below 1 T in all samples studied here (Figures 2, 5–9). Thus, while it is desirable to measure saturation FORC distributions, which is possible with instruments with higher maximum field capabilities, much valuable information is captured in FORC diagrams with ~1 T maximum applied fields.

7. Conclusions

Two main FORC distribution types are obtained for hematite samples: kidney-shaped and ridge-type. Some samples have mixtures of the two. Numerical simulations of noninteracting SD particles and experimental results for a 5-mm crystal demonstrate that the FORC distribution type obtained depends on the balance between uniaxial anisotropies and triaxial anisotropy within the basal plane. Commonly observed uniaxial-type FORC diagrams are consistent with magnetoelastic control of uniaxial strain on the magnetic properties of hematite. The fact that both FORC distribution types are observed commonly, including mixtures of the two within a sample, indicates that natural hematite samples lie either close to a balancing point between in-plane and out-of-plane magnetization switching or that they contain two particle types in which one switching mechanism dominates each particle type. FORC simulations for noninteracting SD particles with triaxial anisotropy contain asymmetric signals below $B_u = 0$. Significant vertical spreading of FORC distributions occurs even when no interactions are present, which is due to the asymmetric FORC response that is further smeared when such responses are summed for particle size distributions. Simulated FORC distributions for multiaxial anisotropy lie within the lower FORC half plane; smearing of the FORC distribution into the upper half plane in experimental FORC distributions requires an explanation that has yet to be simulated with known mechanisms. Thermal activation and exchange anisotropy among intergrown particles are potential factors that need future exploration. Overall, our findings have important implications for FORC interpretation of minerals dominated by multiaxial anisotropy. In particular, the simple coercivity-interaction field framework for interpreting horizontal and vertical FORC distributions do not apply to multiaxial systems.

The dominance of hematite in some sample types (e.g., red beds, deeply weathered regolith, iron ores) provides FORC signals due to hematite that are not masked by the much more strongly magnetic magnetite or maghemite (e.g., Hu et al., 2021; Muxworthy et al., 2005). Our results for synthetic and natural hematite samples provide a

valuable point of comparison for studies of hematite-bearing samples and could contribute to training algorithms to unmix FORC data.

Data Availability Statement

All FORC data used here are archived in Zenodo (https://zenodo.org/record/5662702#.YZHAkS8RoQ8) and will also be uploaded to the Magnetic Information Consortium rock magnetic portal (MagIC; www.earthref.org).

Acknowledgments
We thank Ayako Katayama, Dr Yuichiro Tanaka, and Dr Ulrike Troitzsch for their invaluable practical assistance, and Prof. Penny King for providing the HA samples. This work was supported financially by the National Institute of Advanced Industrial Science and Technology, Ministry of Economy, Trade and Industry, Japan (APR, HO, DH, XZ, RJH, and ARM), which supported PXH and TS, the Australian Research Council through grants DP160100805 and DP200100765 (APR, DH, RJH, and ARM), the European Research Council under the European Union's Seventh Framework Programme (FP/2007–2013)/ERC grant agreement number 320750 (RJH), and the National Natural Science Foundation of China (grants 41922026 and 91858108 to ZXJ and 41920104009 to JHL).

References

Abrajevitch, A., Pillans, B. J., & Roberts, A. P. (2014). Haematite pigmentation events and palaeomagnetic recording: Implications from the Pilbara Print Stone, Western Australia. *Geophysical Journal International*, *199*, 658–672. https://doi.org/10.1093/gji/ggu293

Abrajevitch, A., Pillans, B. J., Roberts, A. P., & Kodama, K. (2018). Magnetic properties and paleomagnetism of Zebra Rock, Western Australia: Chemical remanence acquisition in hematite pigment and Ediacaran geomagnetic field behavior. *Geochemistry, Geophysics, Geosystems*, *19*, 732–748. https://doi.org/10.1002/2017gc007091

Abrajevitch, A., Roberts, A. P., Pillans, B. J., & Hori, R. S. (2021). Unexpected magnetic behavior of natural hematite-bearing rocks at low temperatures. *Geochemistry, Geophysics, Geosystems*, *22*, e2021GC010094. https://doi.org/10.1029/2021GC010094

Anand, R. R., & Butt, C. R. M. (2010). A guide for mineral exploration through the regolith in the Yilgarn Craton, Western Australia. *Australian Journal of Earth Sciences*, *57*, 1015–1114. https://doi.org/10.1080/08120099.2010.522823

Anderson, P. W., Merritt, F. R., Remeika, J. P., & Yager, W. A. (1954). Magnetic resonance in αFe_2O_3. *Physical Review*, *93*, 717–718. https://doi.org/10.1103/physrev.93.717

Banerjee, S. K. (1963). An attempt to observe the basal plane anisotropy of hematite. *Philosophical Magazine*, *8*, 2119–2120. https://doi.org/10.1080/14786436308209106

Banerjee, S. K. (1971). New grain size limits for palaeomagnetic stability in haematite. *Nature Physical Science*, *232*, 15–16. https://doi.org/10.1038/physci232015a0

Berndt, T. A., Chang, L., Wang, S. S., & Badejo, S. (2018). Time-asymmetric FORC diagrams: A new protocol for visualizing thermal fluctuations and distinguishing magnetic mineral mixtures. *Geochemistry, Geophysics, Geosystems*, *19*, 3056–3070. https://doi.org/10.1029/2018gc007669

Bødker, F., Hansen, M. F., Koch, C. B., Lefmann, K., & Mørup, S. (2000). Magnetic properties of hematite nanoparticles. *Physical Review B*, *61*, 6826–6838.

Brok, E., Frandsen, C., Lefmann, K., McEnroe, S., Robinson, P., Burton, B. P., et al. (2017). Experimental evidence for lamellar magnetism in hemo-ilmenite by polarized neutron scattering. *American Mineralogist*, *102*, 1234–1243. https://doi.org/10.2138/am-2017-5792ccby

Brownlee, S. J., Feinberg, J. M., Kasama, T., Harrison, R. J., Scott, G. R., & Renne, P. R. (2011). Magnetic properties of ilmenite-hematite single crystals from the Ecstall pluton near Prince Rupert, British Columbia. *Geochemistry, Geophysics, Geosystems*, *12*, Q07Z29. https://doi.org/10.1029/2011GC003622

Bruzzone, C. L., & Ingalls, R. (1983). Mössbauer-effect study of the Morin transition and atomic positions in hematite under pressure. *Physical Review B*, *28*, 2430–2440. https://doi.org/10.1103/physrevb.28.2430

Carvallo, C., & Muxworthy, A. R. (2006). Low-temperature first-order reversal curve (FORC) diagrams for synthetic and natural samples. *Geochemistry, Geophysics, Geosystems*, *7*, Q09003. https://doi.org/10.1029/2006GC001299

Carvallo, C., Muxworthy, A. R., & Dunlop, D. J. (2006). First-order reversal curve (FORC) diagrams of magnetic mixtures: Micromagnetic models and measurements. *Physics of the Earth and Planetary Interiors*, *154*, 308–322. https://doi.org/10.1016/j.pepi.2005.06.017

Chase, A. B., & Morse, F. L., Jr (1973). Habit of Fe_2O_3 grown from $Na_2B_4O_7$. *Journal of Crystal Growth*, *19*, 18–20. https://doi.org/10.1016/0022-0248(73)90075-4

Chen, Y. H., & Lin, C. C. (2014). Effect of nano-hematite morphology on photocatalytic activity. *Physics and Chemistry of Minerals*, *41*, 727–736. https://doi.org/10.1007/s00269-014-0686-9

Chmiel, F. P., Waterfield Price, N., Johnson, R. D., Lamirand, A. D., Schad, J., van der Laan, G., et al. (2018). Observation of magnetic vortex pairs at room temperature in a planar α-Fe_2O_3/Co heterostructure. *Nature Materials*, *17*, 581–585. https://doi.org/10.1038/s41563-018-0101-x

Church, N. S., Fabian, K., & McEnroe, S. A. (2016). Nonlinear Preisach maps: Detecting and characterizing separate remanent magnetic fractions in complex natural samples. *Journal of Geophysical Research: Solid Earth*, *121*, 8373–8395. https://doi.org/10.1002/2016jb013465

Coey, J. M. D. (2010). *Magnetism and magnetic materials* (pp. 614). Cambridge University Press.

Collinson, D. W. (1969). Investigations into the stable remanent magnetization of sediments. *Geophysical Journal of the Royal Astronomical Society*, *18*, 211–222. https://doi.org/10.1111/j.1365-246x.1969.tb03563.x

Cornell, R. M., & Schwertmann, U. (2003). *The iron oxides: Structure, properties, reactions, occurrences and uses* (pp. 664). Wiley.

Creer, K. M. (1961). Superparamagnetism in red sediments. *Geophysical Journal of the Royal Astronomical Society*, *5*, 16–28.

Cullity, B. D. (1972). *Introduction to magnetic materials* (1st ed., pp. 666). Addison-Wesley.

de Boer, C. B., & Dekkers, M. J. (1998). Thermomagnetic behaviour of haematite and goethite as a function of grain size in various non-saturating magnetic fields. *Geophysical Journal International*, *133*, 541–552. https://doi.org/10.1046/j.1365-246x.1998.00522.x

de Boer, C. B., Mullender, T. A. T., & Dekkers, M. J. (2001). Low-temperature behaviour of haematite: Susceptibility and magnetization increase on cycling through the Morin transition. *Geophysical Journal International*, *146*, 201–216. https://doi.org/10.1046/j.0956-540x.2001.01443.x

Dekkers, M. J. (1990). Magnetic properties of natural goethite—III. Magnetic behaviour and properties of minerals originating from goethite dehydration during thermal demagnetization. *Geophysical Journal International*, *103*, 233–250. https://doi.org/10.1111/j.1365-246x.1990.tb01765.x

Dekkers, M. J., & Linssen, J. H. (1989). Rockmagnetic properties of fine-grained natural low-temperature haematite with reference to remanence acquisition mechanisms in red beds. *Geophysical Journal International*, *99*, 1–18. https://doi.org/10.1111/j.1365-246x.1989.tb02012.x

DiffracPlus Eva software version 10.0. (2004). *DiffracPlus Eva software version 10.0*. Bruker AXS GmbH.

Dormann, J. L., Fiorani, D., & Tronc, E. (1997). Magnetic relaxation in fine-particle systems. *Advances in Chemical Physics*, *98*, 283–494.

Dow, D. B., & Gemuts, I. (1969). *Geology of the Kimberley region*. (Vol. 120). Geological Survey of Western Australia.

Dunlop, D. J. (1970). Hematite: Intrinsic and defect ferromagnetism. *Science*, *169*, 858–860. https://doi.org/10.1126/science.169.3948.858

Dunlop, D. J. (1971). Magnetic properties of fine-particle hematite. *Annales de Géophysique*, *27*, 269–293.

Dunlop, D. J. (1972). Magnetic mineralogy of unheated and heated red sediments by coercivity spectrum analysis. *Geophysical Journal of the Royal Astronomical Society*, *27*, 37–55. https://doi.org/10.1111/j.1365-246x.1972.tb02346.x

Dzyaloshinsky, I. (1958). A thermodynamic theory of "weak" ferromagnetism of antiferromagnetics. *Journal of Physics and Chemistry of Solids*, *4*, 241–255. https://doi.org/10.1016/0022-3697(58)90076-3

Egli, R. (2006). Theoretical aspects of dipolar interactions and their appearance in first-order reversal curves of thermally activated single-domain particles. *Journal of Geophysical Research*, *111*, B12S17. https://doi.org/10.1029/2006JB004567

Egli, R. (2013). VARIFORC: An optimized protocol for the calculation of non-regular first-order reversal curve (FORC) diagrams. *Global and Planetary Change*, *110*, 302–320. https://doi.org/10.1016/j.gloplacha.2013.08.003

Egli, R. (2021). Magnetic characterization of geologic materials with first-order reversal-curves. In V. Franco, & B. Dodrill (Eds.), *Magnetic measurement techniques for materials characterization* (pp. 449–597). Springer Nature Publishing Group. https://doi.org/10.1007/978-3-030-70443-8_17

Egli, R., Chen, A. P., Winklhofer, M., Kodama, K. P., & Horng, C. S. (2010). Detection of noninteracting single domain particles using first-order reversal curve diagrams. *Geochemistry, Geophysics, Geosystems*, *11*, Q01Z11. https://doi.org/10.1029/2009GC002916

Fabian, K. (2003). Some additional parameters to estimate domain state from isothermal remanent magnetization. *Earth and Planetary Science Letters*, *213*, 337–345. https://doi.org/10.1016/s0012-821x(03)00329-7

Fabian, K., Robinson, P., McEnroe, S. A., Heidelbach, F., & Hirt, A. M. (2011). Experimental study of the magnetic signature of basal-plane anisotropy in hematite. In E. Petrovsky (Ed.), *The Earth's magnetic field. IAGA special Sopron book series* (Vol. 1, pp. 311–320). https://doi.org/10.1007/978-94-007-0323-0_22

Flanders, P. J., & Schuele, W. J. (1964). Anisotropy in the basal plane of hematite single crystals. *Philosophical Magazine*, *9*, 485–490. https://doi.org/10.1080/14786436408222959

Fletcher, E. J., & O'Reilly, W. (1974). Contribution of Fe^{2+} ions to the magnetocrystalline anisotropy constant K_1 of $Fe_{3-x}Ti_xO_4$ ($0 < x < 0.1$). *Journal of Physics C: Solid State Physics*, *7*, 171–178. https://doi.org/10.1088/0022-3719/7/1/024

Frank, U., & Nowaczyk, N. R. (2008). Mineral magnetic properties of artificial samples systematically mixed from haematite and magnetite. *Geophysical Journal International*, *175*, 449–461. https://doi.org/10.1111/j.1365-246x.2008.03821.x

Harrison, R. J., & Feinberg, J. M. (2008). FORCinel: An improved algorithm for calculating first-order reversal curve distributions using locally weighted regression smoothing. *Geochemistry, Geophysics, Geosystems*, *9*, Q05016. https://doi.org/10.1029/2008GC001987

Harrison, R. J., & Lascu, I. (2014). FORCulator: A micromagnetic tool for simulating first-order reversal curve diagrams. *Geochemistry, Geophysics, Geosystems*, *15*, 4671–4691. https://doi.org/10.1002/2014gc005582

Harrison, R. J., Zhao, X., Hu, P. X., Sato, T., Heslop, D., Muxworthy, A. R., et al. (2019). Simulation of remanent, transient, and induced FORC diagrams for interacting particles with uniaxial, cubic, and hexagonal anisotropy. *Journal of Geophysical Research: Solid Earth*, *124*(12), 12404–12429. https://doi.org/10.1029/2019jb018050

Horng, C. S. (2018). Unusual magnetic properties of sedimentary pyrrhotite in methane seepage sediments: Comparison with metamorphic pyrrhotite and sedimentary greigite. *Journal of Geophysical Research: Solid Earth*, *123*, 4601–4617. https://doi.org/10.1002/2017jb015262

Horng, C. S., & Roberts, A. P. (2018). The low-temperature Besnus magnetic transition: Signals due to monoclinic and hexagonal pyrrhotite. *Geochemistry, Geophysics, Geosystems*, *19*, 3364–3375. https://doi.org/10.1029/2017gc007394

Hu, P. X., Oda, H., Zhao, X., Harrison, R. J., Heslop, D., Sato, T., et al. (2021). Assessment of magnetic techniques for understanding complex mixtures of magnetite and hematite: The Inuyama red chert. *Journal of Geophysical Research: Solid Earth*, *126*, e2020JB019518. https://doi.org/10.1029/2020JB019518

ICDD. (2004). *PDF-2*. International Centre for Diffraction Data.

Islam, M. S., Kusumoto, Y., & Abdulla-Al-Mamun, M. (2012). Novel rose-type magnetic (Fe_3O_4, γ-Fe_2O_3 and α-Fe_2O_3) nanoplates synthesized by simple hydrothermal decomposition. *Materials Letters*, *66*, 165–167. https://doi.org/10.1016/j.matlet.2011.08.057

Iwata, M. (1965). Magnetic behavior of α-Fe_2O_3, I. Origin of weak ferromagnetism and magnetic characteristics. *Advanced Physics*, *34*, 812–824. (in Japanese with English abstract).

Jiang, Z. X., Liu, Q. S., Barrón, V., Torrent, J., & Yu, Y. J. (2012). Magnetic discrimination between Al-substituted hematites synthesized by hydrothermal and thermal dehydration methods and its geological significance. *Journal of Geophysical Research*, *117*, B02102. https://doi.org/10.1029/2011JB008605

Jiang, Z. X., Liu, Q. S., Dekkers, M. J., Barrón, V., Torrent, J., & Roberts, A. P. (2016). Control of Earth-like magnetic fields on the transformation of ferrihydrite to hematite and goethite. *Scientific Reports*, *6*, 30395. https://doi.org/10.1038/srep30395

Jiang, Z. X., Liu, Q. S., Dekkers, M. J., Colombo, C., Yu, Y. J., Barrón, V., et al. (2014). Ferro and antiferromagnetism of ultrafine-grained hematite. *Geochemistry, Geophysics, Geosystems*, *15*, 2699–2712. https://doi.org/10.1002/2014gc005377

Jiang, Z. X., Liu, Q. S., Dekkers, M. J., Tauxe, L., Qin, H. F., Barrón, V., et al. (2015). Acquisition of chemical remanent magnetization during experimental ferrihydrite-hematite conversion in Earth-like magnetic field—Implications for paleomagnetic studies of red beds. *Earth and Planetary Science Letters*, *428*, 1–10. https://doi.org/10.1016/j.epsl.2015.07.024

Jiang, Z. X., Liu, Q. S., Roberts, A. P., Dekkers, M. J., Barrón, V., Torrent, J., et al. (2021). The magnetic and color reflectance properties of hematite: From Earth to Mars. *Reviews of Geophysics*, *19*, e2020RG000698. https://doi.org/10.1029/2020RG000698

Jovane, L., Yokoyama, E., Seda, T., Burmester, R. F., Trindade, R. I. F., & Housen, B. A. (2011). Rock magnetism of hematitic "bombs" from the Araguainha impact structure, Brazil. *Geochemistry, Geophysics, Geosystems*, *12*, Q12Z34. https://doi.org/10.1029/2011GC003758

Kars, M., & Kodama, K. (2015a). Authigenesis of magnetic minerals in gas hydrate-bearing sediments in the Nankai Trough, offshore Japan. *Geochemistry, Geophysics, Geosystems*, *16*, 947–961. https://doi.org/10.1002/2014gc005614

Kars, M., & Kodama, K. (2015b). Rock magnetic characterization of ferrimagnetic iron sulfides in gas hydrate-bearing marine sediments at Site C0008, Nankai Trough, Pacific Ocean, off-coast Japan. *Earth, Planets, Space*, *67*, 118. https://doi.org/10.1186/s40623-015-0287-y

Kittel, C. (1949). Physical theory of ferromagnetic domains. *Reviews of Modern Physics*, *21*, 541–583. https://doi.org/10.1103/revmodphys.21.541

Kletetschka, G., & Wasilewski, P. J. (2002). Grain size limit for SD hematite. *Physics of the Earth and Planetary Interiors*, *129*, 173–179. https://doi.org/10.1016/s0031-9201(01)00271-0

Kodama, R. H. (1999). Magnetic nanoparticles. *Journal of Magnetism and Magnetic Materials*, *200*, 359–372. https://doi.org/10.1016/s0304-8853(99)00347-9

Lagroix, F., & Guyodo, Y. (2017). A new tool for separating the magnetic mineralogy of complex mineral assemblages from low temperature magnetic behaviour. *Frontiers in Earth Science*, *5*, 61. https://doi.org/10.3389/feart.2017.00061

Larrasoaña, J. C., Roberts, A. P., Musgrave, R. J., Gràcia, E., Piñero, E., Vega, M., et al. (2007). Diagenetic formation of greigite and pyrrhotite in marine sedimentary systems containing gas hydrates. *Earth and Planetary Science Letters*, *261*, 350–366.

Liu, Q. S., Barrón, V., Torrent, J., Qin, H., & Yu, Y. J. (2010). The magnetism of micro-sized hematite explained. *Physics of the Earth and Planetary Interiors*, *183*, 387–397. https://doi.org/10.1016/j.pepi.2010.08.008

Martín-Hernández, F., & Guerrero-Suárez, S. (2012). Magnetic anisotropy of hematite natural crystals: High field experiments. *International Journal of Earth Science*, *101*, 637–647.
Mizushima, K., & Iida, S. (1966). Effective in-plane anisotropy field in α-Fe_2O_3. *Journal of the Physical Society of Japan*, *21*, 1521–1526. https://doi.org/10.1143/jpsj.21.1521
Morin, F. J. (1950). Magnetic susceptibility of αFe_2O_3 and αFe_2O_3 with added titanium. *Physical Review*, *78*, 819–820. https://doi.org/10.1103/physrev.78.819.2
Moriya, T. (1960). Anisotropic superexchange interaction and weak ferromagnetism. *Physical Review*, *120*, 91–98. https://doi.org/10.1103/physrev.120.91
Muench, G. H., Arajs, S., & Matijevic, E. (1985). The Morin transition in small α-Fe_2O_3 particles. *Physica Status Solidi A*, *92*, 187–192. https://doi.org/10.1002/pssa.2210920117
Muxworthy, A. R., Heslop, D., & Williams, W. (2004). Influence of magnetostatic interactions on first-order-reversal-curve (FORC) diagrams: A micromagnetic approach. *Geophysical Journal International*, *158*, 888–897. https://doi.org/10.1111/j.1365-246x.2004.02358.x
Muxworthy, A. R., King, J. G., & Heslop, D. (2005). Assessing the ability of first-order reversal curve (FORC) diagrams to unravel complex magnetic signals. *Journal of Geophysical Research: Solid Earth*, *110*, B01105. https://doi.org/10.1029/2004JB003195
Néel, L. (1953). Some new results on antiferromagnetism and ferromagnetism. *Reviews of Modern Physics*, *25*, 58–63.
Néel, L. (1954). Remarques sur la théorie des propriétés magnétiques des substances dures. *Applied Scientific Research, Section B*, *4*, 13–24.
Newell, A. J. (2005). A high-precision model of first-order reversal curve (FORC) functions for single-domain ferromagnets with uniaxial anisotropy. *Geochemistry, Geophysics, Geosystems*, *6*, Q05010. https://doi.org/10.1029/2004GC000877
Nininger, R. C., Jr., & Schroeer, D. (1978). Mössbauer studies of the Morin transition in bulk and microcrystalline α-Fe_2O_3. *Journal of Physics and Chemistry of Solids*, *39*, 137–144. https://doi.org/10.1016/0022-3697(78)90213-5
O'Neill, H. S. C., Annersten, H., & Virgo, D. (1992). The temperature dependence of the cation distribution in magnesioferrite ($MgFe_2O_4$) from powder XRD structural refinements and Mössbauer spectroscopy. *American Mineralogist*, *77*, 725–740.
Özdemir, Ö., & Dunlop, D. J. (2014). Hysteresis and coercivity in hematite. *Journal of Geophysical Research: Solid Earth*, *119*, 2582–2594.
Pariona, N., Camacho-Aguilar, K. I., Ramos-González, R., Martinez, A. I., Herrera-Trejo, M., & Baggio-Saitovitch, E. (2016). Magnetic and structural properties of ferrihydrite/hematite nanocomposites. *Journal of Magnetism and Magnetic Materials*, *406*, 221–227. https://doi.org/10.1016/j.jmmm.2016.01.001
Pike, C. R., Roberts, A. P., & Verosub, K. L. (1999). Characterizing interactions in fine magnetic particle systems using first order reversal curves. *Journal of Applied Physics*, *85*, 6660–6667. https://doi.org/10.1063/1.370176
Pike, C. R., Roberts, A. P., & Verosub, K. L. (2001). First-order reversal curve diagrams and thermal relaxation effects in magnetic particles. *Geophysical Journal International*, *145*, 721–730. https://doi.org/10.1046/j.0956-540x.2001.01419.x
Porath, H. (1968). Stress induced magnetic anisotropy in natural single crystals of hematite. *Philosophical Magazine*, *17*, 603–608. https://doi.org/10.1080/14786436808217746
Porath, H., & Raleigh, C. B. (1967). An origin of the triaxial basal-plane anisotropy in hematite crystals. *Journal of Applied Physics*, *38*, 2401–2402. https://doi.org/10.1063/1.1709904
Preisach, F. (1935). Über die magnetische Nachwirkung. *Zeitschrift für Physik*, *94*, 277–302. https://doi.org/10.1007/bf01349418
Rietveld, H. M. (1969). A profile refinement method for nuclear and magnetic structures. *Journal of Applied Crystallography*, *2*, 65–71. https://doi.org/10.1107/s0021889869006558
Roberts, A. P., Almeida, T. P., Church, N. S., Harrison, R. J., Heslop, D., Li, Y. L., et al. (2017). Resolving the origin of pseudo-single domain magnetic behavior. *Journal of Geophysical Research: Solid Earth*, *122*, 9534–9558. https://doi.org/10.1002/2017jb014860
Roberts, A. P., Chang, L., Heslop, D., Florindo, F., & Larrasoaña, J. C. (2012). Searching for single domain magnetite in the 'pseudo-single-domain' sedimentary haystack: Implications of biogenic magnetite preservation for sediment magnetism and relative paleointensity determinations. *Journal of Geophysical Research*, *117*, B08104. https://doi.org/10.1029/2012JB009412
Roberts, A. P., Florindo, F., Larrasoaña, J. C., O'Regan, M. A., & Zhao, X. (2010). Complex polarity pattern at the (former) Plio-Pleistocene global stratotype section at Vrica (Italy): Remagnetization by magnetic iron sulphides. *Earth and Planetary Science Letters*, *292*, 98–111. https://doi.org/10.1016/j.epsl.2010.01.025
Roberts, A. P., Heslop, D., Zhao, X., & Pike, C. R. (2014). Understanding fine magnetic particle systems through use of first-order reversal curve diagrams. *Reviews of Geophysics*, *52*, 557–602. https://doi.org/10.1002/2014rg000462
Roberts, A. P., Liu, Q. S., Rowan, C. J., Chang, L., Carvallo, C., Torrent, J., et al. (2006). Characterization of hematite (α-Fe_2O_3), goethite (α-FeOOH), greigite (Fe_3S_4), and pyrrhotite (Fe_7S_8) using first-order reversal curve diagrams. *Journal of Geophysical Research: Solid Earth*, *111*, B12S35. https://doi.org/10.1029/2006JB004715
Roberts, A. P., Pike, C. R., & Verosub, K. L. (2000). First-order reversal curve diagrams: A new tool for characterizing the magnetic properties of natural samples. *Journal of Geophysical Research: Solid Earth*, *105*(B12), 28461–28475. https://doi.org/10.1029/2000jb900326
Roberts, A. P., Zhao, X., Heslop, D., Abrajevitch, A., Chen, Y.-H., Hu, P. X., et al. (2020). Hematite (α-Fe_2O_3) quantification in sedimentary magnetism: Limitations of existing proxies and ways forward. *Geoscience Letters*, *7*, 8. https://doi.org/10.1186/s40562-020-00157-5
Robinson, P., Harrison, R. J., McEnroe, S. A., & Hargraves, R. B. (2004). Nature and origin of lamellar magnetism in the hematite-ilmenite series. *American Mineralogist*, *89*, 725–747. https://doi.org/10.2138/am-2004-5-607
Samuelson, E. J., & Shirane, G. (1970). Inelastic neutron scattering investigation of spin waves and magnetic interactions in α-Fe_2O_3. *Physica Status Solidi*, *42*, 241–256.
Schabes, M. E., & Bertram, H. N. (1988). Magnetization processes in ferromagnetic cubes. *Journal of Applied Physics*, *64*, 1347–1357. https://doi.org/10.1063/1.341858
Searle, C. W. (1967). On the pressure dependence of low-temperature transition in hematite. *Physics Letters A*, *25*, 256–257. https://doi.org/10.1016/0375-9601(67)90890-0
Shull, C. G., Strauser, W. A., & Wollan, E. O. (1951). Neutron diffraction by paramagnetic and antiferromagnetic substances. *Physical Review*, *83*, 333–345. https://doi.org/10.1103/physrev.83.333
Stacey, F. D., & Banerjee, S. K. (1974). *The physical principles of rock magnetism* (pp. 195). Elsevier.
Stokking, L., & Tauxe, L. (1990). Properties of chemical remanence in synthetic hematite: Testing theoretical predictions. *Journal of Geophysical Research: Solid Earth*, *95*(B8), 12639–12652. https://doi.org/10.1029/jb095ib08p12639
Stoner, E. C., & Wohlfarth, E. P. (1948). A mechanism of magnetic hysteresis in heterogeneous alloys. *Philosophical Transactions of the Royal Society of London A*, *240*, 599–642.
Sunagawa, I., & Flanders, P. J. (1965). Structural and magnetic studies in hematite single crystals. *Philosophical Magazine*, *11*, 747–761. https://doi.org/10.1080/14786436508230080

Tasaki, A., & Iida, S. (1963). Magnetic properties of synthetic single crystal of αFe_2O_3. *Journal of the Physical Society of Japan*, *18*, 1148–1154. https://doi.org/10.1143/jpsj.18.1148

Tauxe, L., Butler, R., Banerjee, S. K., & van der Voo, R. (2010). *Essentials of paleomagnetism* (pp. 512). University of California Press. Retrieved from https://earthref.org/MagIC/books/Tauxe/Essentials/

Tauxe, L., Santos, C. N., Cych, B., Zhao, X., Roberts, A. P., Nagy, L., et al. (2021). Understanding nonideal paleointensity recording in igneous rocks: Insights from aging experiments on lava samples and the causes and consequences of "fragile" curvature in Arai plots. *Geochemistry, Geophysics, Geosystems*, *22*, e2020GC009423. https://doi.org/10.1029/2020GC009423

Urquhart, H. M. A., & Goldman, J. E. (1956). Magnetostrictive effects in an antiferromagnetic haematite crystal. *Physical Review*, *101*, 1443–1450. https://doi.org/10.1103/physrev.101.1443

Valdez-Grijalva, M. A., & Muxworthy, A. R. (2019). First-order reversal curve (FORC) diagrams of nanomagnets with cubic magnetocrystalline anisotropy: A numerical approach. *Journal of Magnetism and Magnetic Materials*, *471*, 359–364. https://doi.org/10.1016/j.jmmm.2018.09.086

Valdez-Grijalva, M. A., Muxworthy, A. R., Williams, W., Ó Conbhuí, P., Nagy, L., Roberts, A. P., et al. (2018). Magnetic vortex effects on first-order reversal curve (FORC) diagrams for greigite dispersions. *Earth and Planetary Science Letters*, *501*, 103–111. https://doi.org/10.1016/j.epsl.2018.08.027

Verwey, E. J. W. (1939). Electronic conduction of magnetite (Fe_3O_4) and its transition point at low temperatures. *Nature*, *144*, 327–328. https://doi.org/10.1038/144327b0

Weaver, R., Roberts, A. P., & Barker, A. J. (2002). A late diagenetic (syn-folding) magnetization carried by pyrrhotite: Implications for paleomagnetic studies from magnetic iron sulphide-bearing sediments. *Earth and Planetary Science Letters*, *200*, 371–386. https://doi.org/10.1016/s0012-821x(02)00652-0

Wehland, F., Stancu, A., Rochette, P., Dekkers, M. J., & Appel, E. (2005). Experimental evaluation of magnetic interaction in pyrrhotite bearing samples. *Physics of the Earth and Planetary Interiors*, *153*, 181–190. https://doi.org/10.1016/j.pepi.2005.05.006

Williams, W., & Dunlop, D. J. (1989). Three-dimensional micromagnetic modelling of ferromagnetic domain structure. *Nature*, *337*, 634–637. https://doi.org/10.1038/337634a0

Wohlfarth, E. P. (1955). The remanent magnetization of haematite powders. *Philosophical Magazine*, *46*, 1155–1164. https://doi.org/10.1080/14786441108520628

Zhao, X., Heslop, D., & Roberts, A. P. (2015). A protocol for variable-resolution first-order reversal curve measurements. *Geochemistry, Geophysics, Geosystems*, *16*, 1364–1377. https://doi.org/10.1002/2014gc005680

Zhao, X., Roberts, A. P., Heslop, D., Paterson, G. A., Li, Y. L., & Li, J. H. (2017). Magnetic domain state diagnosis using hysteresis reversal curves. *Journal of Geophysical Research: Solid Earth*, *122*, 4767–4789. https://doi.org/10.1002/2016jb013683